THESIS FOR THE DEGREE OF LICENTIATE OF ENGINEERING

Detection and classification of internal flaws in laser powder bed fusion

Application of in-situ monitoring for quality control of Hastelloy X builds

CLAUDIA SCHWERZ

Department of Industrial and Materials Science

CHALMERS UNIVERSITY OF TECHNOLOGY

Gothenburg, Sweden 2021

Detection and classification of internal flaws in laser powder bed fusion: Application of in-situ monitoring for quality control of Hastelloy X builds

CLAUDIA SCHWERZ

© CLAUDIA SCHWERZ, 2021

Licentiate thesis at Chalmers University of Technology

Report no. IMS-2021-12

Department of Industrial and Materials Science

Chalmers University of Technology

SE-412 96 Gothenburg

Sweden

Telephone + 46 (0)31-772 1000

Printed by Chalmers Reproservice

Gothenburg, Sweden 2021

Detection and classification of internal flaws in laser powder bed fusion: Application of in-situ monitoring for quality control of Hastelloy X builds

CLAUDIA SCHWERZ

Department of Industrial and Materials Science

Chalmers University of Technology

ABSTRACT

Additive manufacturing technologies, in particular laser powder bed fusion (LPBF), have received much attention in recent years due to their multiple advantages over traditional manufacturing. Yet, the usage of additively manufactured products is still quite limited, mainly due to two factors: the low repeatability, which is particularly relevant for applications where high performance is required from the materials, and the typically low productivity, particularly relevant for products with a substantial production volume.

The main factor that affects repeatability and compromises the performance of the materials is the presence of flaws. Hence, to assess the quality of a product and to predict its performance, it is crucial to recognize which flaws are present and ensure their detectability. Moreover, if the flaws can be detected during the manufacturing process, corrective actions can be taken. In this thesis, internal flaws were deliberately created in LPBF manufactured material to assess their detectability via in-situ monitoring. Two main routes of deliberate flaw formation have been identified while preserving flaw formation mechanisms; therefore, this thesis is split into two parts, according to the approach employed to create flaws.

Flaws are generated systematically if inadequate process parameters are employed. By varying the processing conditions, different types, amounts and sizes of flaws are created. By monitoring the manufacturing process with long-exposure near-infrared imaging and applying supervised machine learning, it was possible to distinguish process conditions that generate the different flaw categories with accuracy, precision and recall of at least 96%.

Flaws are created stochastically as a result of the redeposition of process by-products on the build area. It was found that substantial amounts of flaws can be provoked through this route when increasing the nominal layer thickness in the build, thus enabling the validation of the monitoring system in their detection. After applying an image analysis algorithm to all the images output from in-situ monitoring in three builds, it was possible to identify trends in the spatial distribution of spatter redeposits. Ex-situ inspection and material characterization provided cross-check for the distribution of flaws.

The low productivity of LPBF makes it less competitive in applications with moderate to high production volumes. This issue is briefly addressed in this thesis. Even though one of the main approaches to increase productivity is to tune the main process parameters, dissimilar strategies were identified in the literature towards this goal. Thus, parametrization of build rates was done and applied to the processing conditions deemed to provide material with acceptable quality, based on the quantity and types of flaws present. The material manufactured in these conditions was characterized, and it was found that substantially different microstructures can be achieved within the process window, depending on the build rate.

Keywords: Additive manufacturing; powder bed fusion; process monitoring; flaw detection; defects; lack of fusion; pores; spatter; melt pool; nickel-based superalloy; productivity

PREFACE

The work presented in this licentiate thesis was conducted at the Department of Industrial and Materials Science at Chalmers University of Technology between April 2019 and July 2021 under the supervision of Professor Lars Nyborg. The work was conducted within the framework of the project MANUELA - Additive Manufacturing using Metal Pilot Line (H2020 Grant No. 820774) and in the Centre for Additive Manufacturing – Metal (CAM2), supported by Vinnova.

List of Appended Papers

Paper I ***Linking in-situ melt pool monitoring to melt pool size distributions and internal flaws in laser powder bed fusion***

C. Schwerz, L. Nyborg

Manuscript submitted for publication.

Paper II ***Identification of internal flaws in laser powder bed fusion by a neural network employed on near-infrared long-exposure images acquired by in-situ monitoring***

C. Schwerz, L. Nyborg

Manuscript.

Paper III ***Increasing productivity of laser powder bed fusion manufactured Hastelloy X through modification of process parameters***

C. Schwerz, F. Schulz, L. Nyborg

Manuscript. To be presented at Euromat 2021.

Paper IV ***In-situ detection of redeposited spatter and its influence on the formation of internal flaws in laser powder bed fusion***

C. Schwerz, A. Raza, X. Lei, L. Nyborg, E. Hryha, H. Wirdelius

Manuscript submitted for publication.

Contribution to Appended Papers

Paper I The author conceptualized the work, planned and executed the experimental work and analysis of the results. The author wrote the paper in collaboration with the co-author.

Paper II The author conceptualized the work, planned and executed the experimental work and analysis of the results. The author wrote the paper in collaboration with the co-author.

Paper III The author conceptualized the work, planned and executed the AM experimental work. Dr. Fiona Schulz conducted the EBSD analysis. The author wrote the paper in collaboration with the co-authors.

Paper IV The author conceptualized the work, planned and executed the AM experimental work and image analysis. Ahmad Raza conducted the SEM and XPS analysis. Xiangyu Lei conducted the ultrasonic inspection. The author wrote the paper in collaboration with the co-authors.

CONTENTS

CHAPTER 1
INTRODUCTION

1.1 Background

Additive manufacturing (AM) comprises a range of production technologies based on a bottom-up approach to product manufacturing. Fabrication is performed layer upon layer, opposed to traditional manufacturing methods, also called subtractive, based on material removal for shaping material blocks into final parts.

One of the main advantages of AM in comparison with traditional methods is the increased design flexibility that enables the production of geometrically complex structures that would not be feasible through traditional manufacturing. The expanded design freedom also entails possibilities to reduce the amount of material needed to produce a component while maintaining its functions, which is particularly relevant to sectors such as aerospace and automotive, where lighter structures translate into less fuel consumption, apart from reduced material and cost.

AM enables the reduction or elimination of support components (for example, molds and cutting tools) needed for manufacturing. In some cases, even the need for joining processes and complex supply chains is eliminated by producing a component in a reduced number of steps. Furthermore, the amount of waste generated in AM is reduced compared to traditional methods, not only due to the capability of producing near net shape parts, but also to the possibility of on-demand manufacturing that minimizes the number of products going unsold.

However, for society to enjoy all the benefits this group of technologies can bring, additive manufacturing must reach a broader range of industrial segments and apply to a broader range of products, still complying with quality requirements. Two of the main issues hindering the widespread adoption of AM are the low reliability of AM-manufactured products, a factor particularly relevant for components with high added value and stringent requirements, and low productivity, particularly relevant for mass-produced components.

While no manufacturing method can produce flaw-free parts, traditional manufacturing methods have reached a maturity level in which the main flaw formation mechanisms are understood, appropriate detection procedures have been formulated, mitigation strategies have been developed, tested and implemented exhaustively, and lastly, tolerance limits for flaws have been established for a given application. In AM, quality control processes must be implemented in a similar fashion. As AM technologies are relatively new compared to traditional manufacturing methods, some steps towards the implementation of components produced through this route are still lacking. Many flaw formation mechanisms have been

elucidated, but there is much room for development in the detection and mitigation of flaws. The layer-by-layer nature of the process represents a potentiality in the mitigation of flaws that is not encountered in traditional manufacturing. Once the capability of monitoring systems to detect flaws during the manufacturing process can be demonstrated, corrective actions can be implemented, taking advantage of the subsequent layer in the manufacturing process to heal the flaw.

Furthermore, full post-manufacturing inspection of geometrically complex AM components via non-destructive testing can demand prohibitive amounts of time and resources, or can even be impossible due to technical challenges. A well-calibrated and validated in-situ monitoring system is expected to be capable of detecting flaws regardless of part geometry and to enable the implementation of corrective actions.

1.2 Aims

This thesis has been conducted within the framework of the project MANUELA (H2020 Grant No. 820774), which aims to develop a metal additive manufacturing pilot line service covering the entire AM development cycle, including simulation, robust manufacturing, online process control, real-time feedback, characterization, post-processing and AM qualification protocols [1]. This thesis addresses quality control through process monitoring focused on the detection of internal flaws. This thesis aims to aid overcoming the currently limited reliability in the process, particularly in industries with tight requirements on flaws and the lack of repeatability in the material properties, which stems from flaws. The vision includes addressing the limited capability of right-first-time production by implementing closed-loop control, i.e., automatic detection and mitigation of flaws. The issue of low productivity in LBPF manufacturing is also addressed briefly.

1.3 Research questions

The research questions formulated from the aims of this thesis are:

- RQ1: Which internal flaw types occur in LPBF manufactured Hastelloy X?
- RQ2: Can internal flaws be detected through process monitoring?
- RQ3: Can stochastic flaws be attributed to spatter redeposition on the powder bed?
- RQ4: Can the productivity of LPBF be increased without compromising quality?

1.4 Scope and limitations

The definition of *flaws* can be broad and include factors such as geometrical deviations and surface roughness. The assessment of these factors would branch off this research to the appraisal of design aspects, in-depth studies of the thermal history and residual stresses, evaluation of additional process parameters, and multiple post-processing routes. As these

factors largely widen the scope, this thesis addresses internal flaws only, which include lack of fusion, porosity, and cracks. The term *flaw* is consistently used through this thesis to designate a discontinuity in the material, such as lack of fusion and pores. The term *defect* is avoided as it denotes rejectability based on acceptance standards or specifications particular to a product or application [2].

The material selected for this study is the nickel-based superalloy Hastelloy X. This alloy has been selected due to its good printability and relatively simple metallurgy in comparison to other superalloys and because avoidance of flaws is fundamental in the usual applications area of this alloy. Since Hastelloy X is an alloy containing a single phase and not prone to metallurgical cracking, factors extrinsic to the alloy responsible for the formation of flaws can be more easily isolated, thereby enhancing the control and detection of deliberately created flaws. It should be noted that there are reports in the literature that Hastelloy X can be susceptible to cracking in LPBF, but according to the results, experience and practice maintained in this thesis study, this is issue has not been identified.

In this thesis, the focus is given to the characterization and detection of internal flaws in the material. Microstructural characterization is performed only for material virtually free from flaws. Topics such as design and post-processing, including surface and heat treatment, are not addressed, and the assessment of surface flaws is not a part of the study.

CHAPTER 2
LASER POWDER BED FUSION

2.1 Metal additive manufacturing

Metal additive manufacturing processes consolidate metallic materials in powder, wire or sheet form into dense parts by melting with the aid of an energy source and subsequent solidification in a layer by layer manner [3]. Metal AM technologies can be divided into two broad categories, directed energy deposition, in which energy is used to fuse materials as they are being deposited, and powder bed fusion, in which thermal energy selectively fuses regions of thin powder layers spread on the build area [4]. Powder bed processes are distinguished by the energy source employed, electron beam or laser [5]. This thesis is dedicated to the study of powder bed metal additive manufacturing employing laser as the source of energy, that is, laser powder bed fusion (LPBF).

2.2 Laser powder bed fusion

Hardware and working principle

The main steps in laser powder bed fusion manufacturing are [6]:

(1) creation of a 3D model that describes the part geometry;

(2) preparation of the build, which includes the positioning of the part on the build area, addition of support structures where necessary, and machine setup;

(3) the manufacturing process, conducted by spreading a thin powder layer on a build platform and selectively melting according to the part geometry on that layer; lowering the build platform and repeating the process until the part is completed;

(4) post-processing steps such as cutting the built part from the platform, removal of support structures, and heat and surface treatments.

The hardware utilized in laser powder bed fusion is schematized in Figure 1, including the monitoring systems utilized in this thesis, which will be described in detail in Section 7.3 The equipment consists of a powder dispenser that is elevated at each layer to provide powder that is spread on the build platform by the recoater. Excess powder is carried by the recoater to the powder collector. The laser source, often an ytterbium fiber laser in LPBF, is located outside the build chamber. The laser beam travels through an optical system, is focused with an F-theta lens, and enters the build chamber to expose the regions of the powder bed that correspond to the geometrical model in each layer.

Each laser source has a maximum nominal power, but the effective laser power P employed on exposure is user-defined and is one of the main process parameters. Upon exposure, the laser travels at a velocity (or scan speed) v, to completely scan the area defined by the 3D model in that layer according to a pre-defined pattern (hatch pattern), where two neighboring tracks are separated by a hatch distance h. One of the most used laser exposure patterns, the stripe pattern, is schematized on the insert in Figure 1. Once the layer is completed, the build platform is lowered, the powder dispenser is raised, the recoater spreads a new powder layer of thickness t, and the process is repeated. The entire process is conducted in an inert gas environment, which is maintained by a gas flow that enters the build chamber through the gas inlet.

Specific regions of the part can be assigned special process parameters. The part boundaries on each layer can be scanned by the laser according to pre-defined contour parameters, and regions on top of which no further layers will be deposited can be assigned a set of *upskin* parameters, which contribute to a better surface finish. Regions that are not directly supported by previous layers or by the build plate are called overhangs and can be exposed by a set of *downskin* parameters.

Physical principle

Upon the interaction with the laser, the feedstock powder, typically in the size range 10 – 60 μm, and the substrate are fused, forming a pool of molten material. Melt pools can have different shapes and sizes depending on the acting heat transfer mechanism. In conduction fusion, the energy is deposited on the surface of the piece and transferred to its interior by conduction [7], resulting in melt pools with semicircular cross-sections (Figure 2A). If electron beams or, as is the case for LPBF, lasers are used as the energy source, high energy densities are attainable [7], causing some alloying elements to evaporate. Multiple reflections of the laser occur in the vapor cavity, thus enabling higher energy absorption [8] and forming a deeper melt pool (Figure 2B). The process is sustained by the competing vapor pressure, which acts to keep the keyhole open, and the pressure from gravitational forces and surface tension, which act to close the keyhole [9]. The fluid flow in the melt pools is governed by Marangoni convection, in which the temperature variation in the melt pool generates a spatial gradient of surface tension [8].

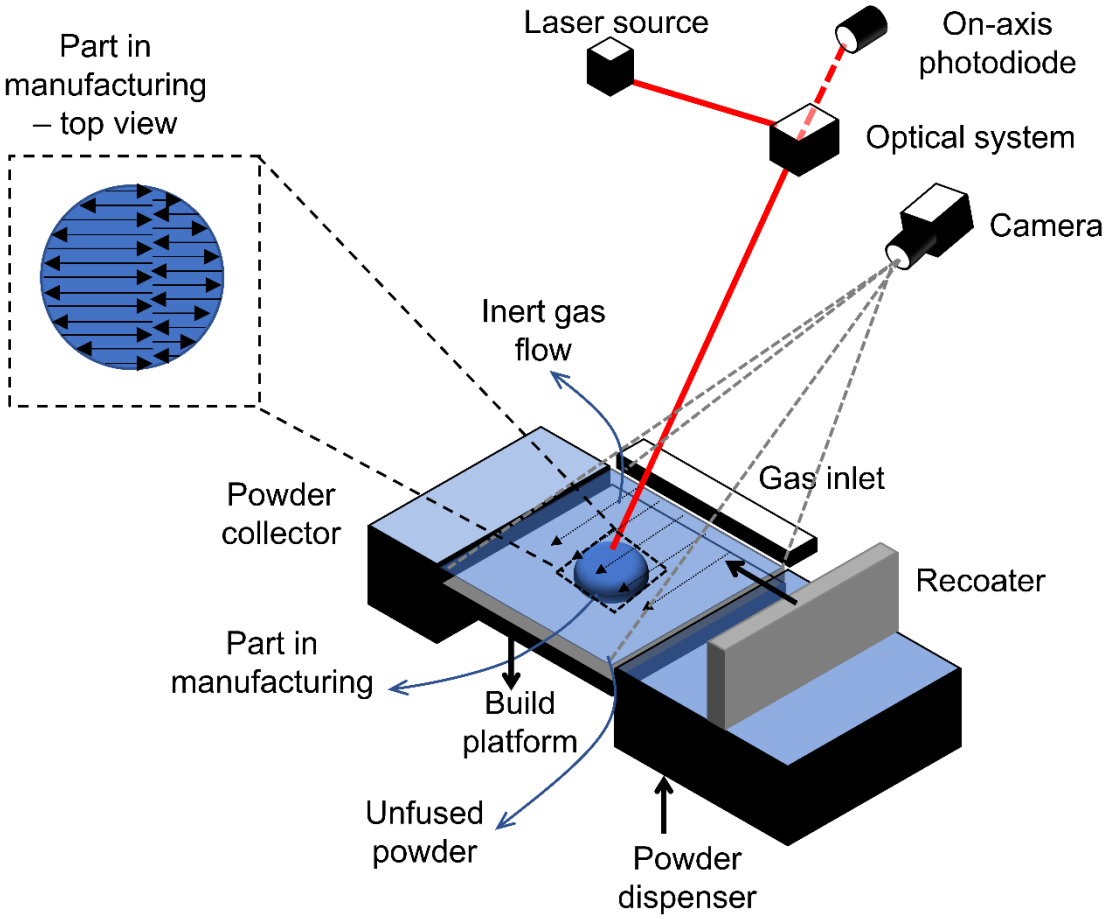

Figure 1 Schematic laser powder bed fusion hardware with the monitoring systems utilized in this thesis. The insert illustrates the top view of a part in manufacturing and schematizes the laser scan vectors following a stripe exposure pattern.

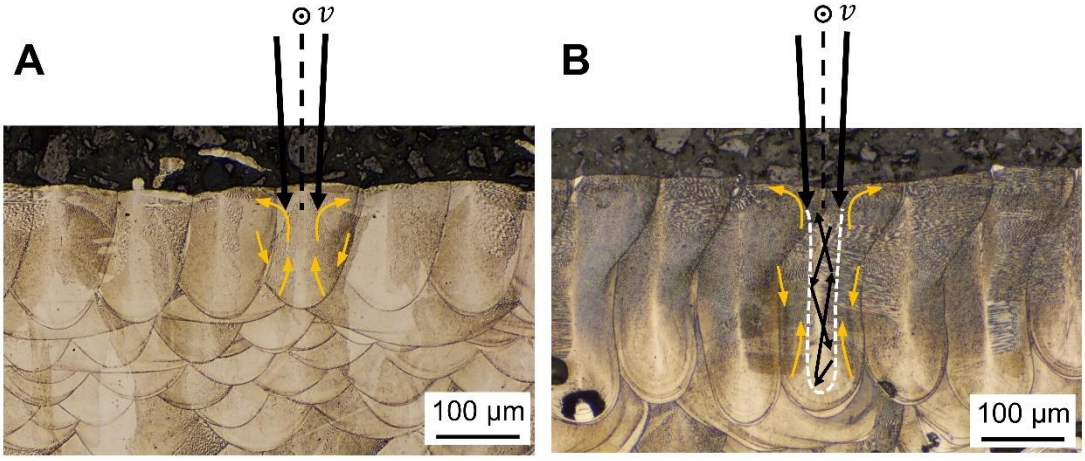

Figure 2 Scheme of fluid flow overlapped to micrographs of melt pools generated in the conduction (A) and keyhole (B) regimes. The laser beam and its travel directions are represented in black. In (B), the vapor cavity is represented with a white dashed line, based on the observations in [10].

2.3 Productivity

The low build rates of laser powder bed fusion represent a major obstacle for its broad application as an industrial manufacturing technology [11] [12] [13]. The low productivity makes the technology more expensive, therefore less competitive in many branches of industry [14] and largely limited to high-end applications with low production volumes, for which elevated costs are acceptable [15]. In order to address this issue, different strategies have been investigated and can be split into two categories: modification of the hardware and modification of the process parameters. Approaches based on hardware modification include the implementation of multiple laser sources [14], or laser sources of increased power [16] [17], that enable instantly processing a large volume of material. This aspect of productivity increase is not addressed in this thesis. The modification of process parameters is a readily available strategy for the enhancement of productivity [11] [18] and can be used to boost the production potential of any LPBF system. However, in this approach, care must be taken to limit the formation of flaws so that gains in productivity do not come at the expense of material quality.

CHAPTER 3
FLAWS IN LASER POWDER BED FUSION

3.1 Definition and classification

According to some authors, the definition of flaws can include geometrical deviations, residual stresses and surface roughness [19]. As the study of single tracks is often a precursor in many AM topics, discontinuous features they may present, such as balling, have also been denominated "flaws" or "defects" in the literature [20] [21]. This work is dedicated to studying internal flaws in multilayer builds, which include cracks, lack of fusion, keyhole porosity and gas porosity.

In keyhole fusion, the deep and narrow vapor cavity created allows more efficient use of energy due to the multiple reflections of the laser in this cavity [10]. However, if keyhole fusion is not controlled, incomplete collapse of the vapor cavity can occur, leaving voids consisting of entrapped vapor [22], also denominated keyhole porosity. In the conduction regime, the relatively smaller melt pools increase the odds of formation of lack of fusion, which originate from the insufficient overlap of neighboring melt pools [23]. Residual gas pores, which are spherical and relatively small, are always expected in the as-built material due to the presence of entrapped gas in the feedstock powder [24] and solubility drop of gas-forming elements present in the feedstock powder upon solidification [25] [26].

Flaws can be classified differently, for example, based on their origin: induced by equipment, feedstock, design or process [19]. In this thesis, the classification is based on the incidence and distribution of flaws, i.e., if they are created systematically or stochastically. This choice is made since the primary aim of this work, the use of monitoring systems for flaw detection, is dependent on the deliberate creation of flaws in a controlled manner. A similar classification system has been utilized in the review article by Snow et al. [25]. The manner by which flaws are created affects their distribution, size, and type, requiring distinct approaches for their detection and resulting in distinct impacts on the material performance.

3.2 Systematic flaws

Flaws are systematically created in LPBF if inadequate combinations of process parameters are selected for manufacturing. Systematic flaws can consist of keyhole porosity, gas porosity, and lack of fusion, and can occur at diverse degrees of severity, as illustrated in Figure 3. Such flaws are uniformly distributed throughout the material.

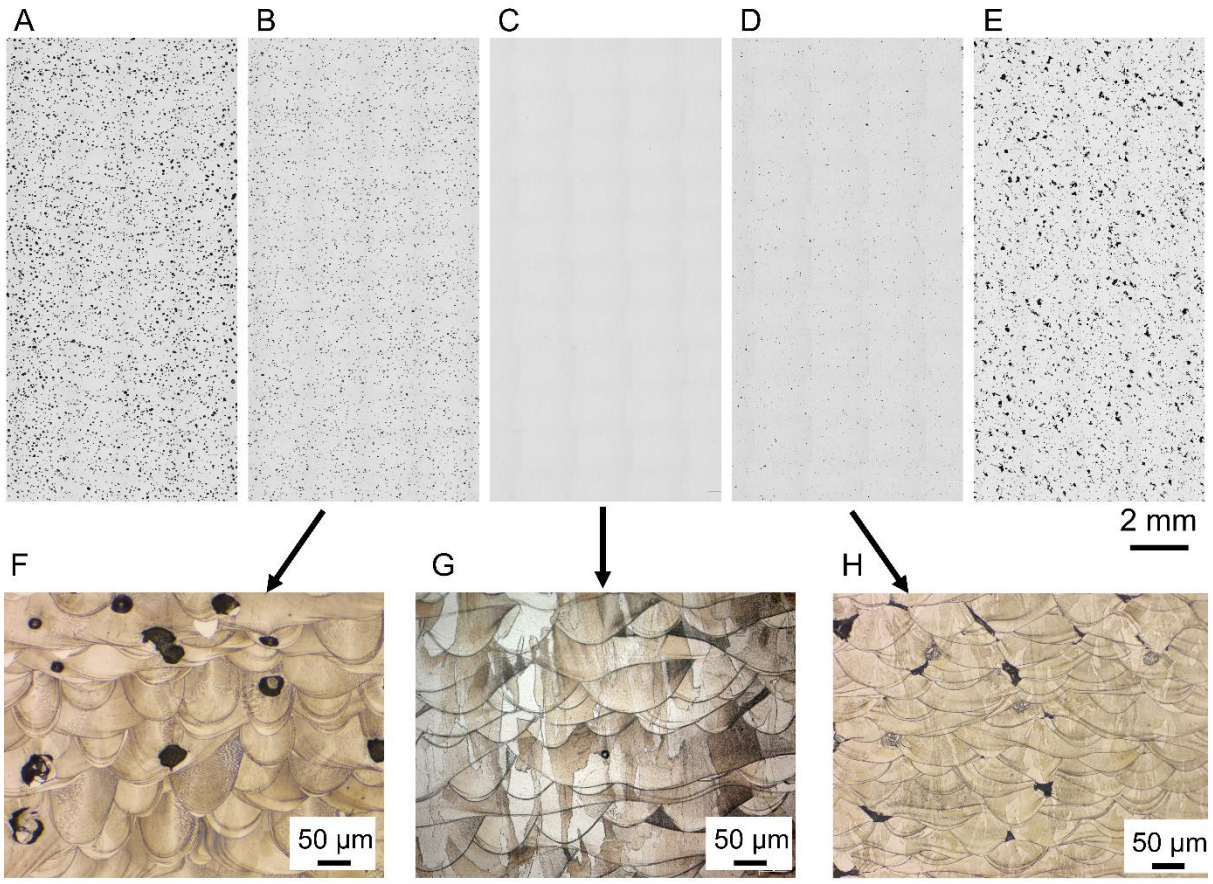

Figure 3 Cross-sections of samples containing systematic flaws. (A) and (B) show systematic keyhole porosity with different degrees of severity. A detailed sample of keyhole porosity is observed in (F). (C) shows a sample virtually free from flaws, in which only gas porosity has been identified. A sample of gas porosity is seen in (G). (D) and (E) show systematic lack of fusion with different degrees of severity. A detailed sample of lack of fusion is observed in (H). From **Paper II**. Results from experiments on Hastelloy X built in EOS M290 LPBF machine.

3.3 Stochastic flaws

Internal flaws can form stochastically in LPBF as a result of, for example, irregularities in the spreading of powder, irregularities in the powder packing, and process by-products [25]. Differently from systematic flaws, the incidence and distribution of stochastic flaws can, in principle, not be anticipated, as their formation is not driven (albeit can be influenced) by user-defined parameters. The distribution of stochastic flaws is irregular, as illustrated in Figure 4, which shows cross-sections of specimens manufactured at invariable processing conditions. In this thesis, the focus is given to stochastic flaws induced by process by-products, more specifically spatter.

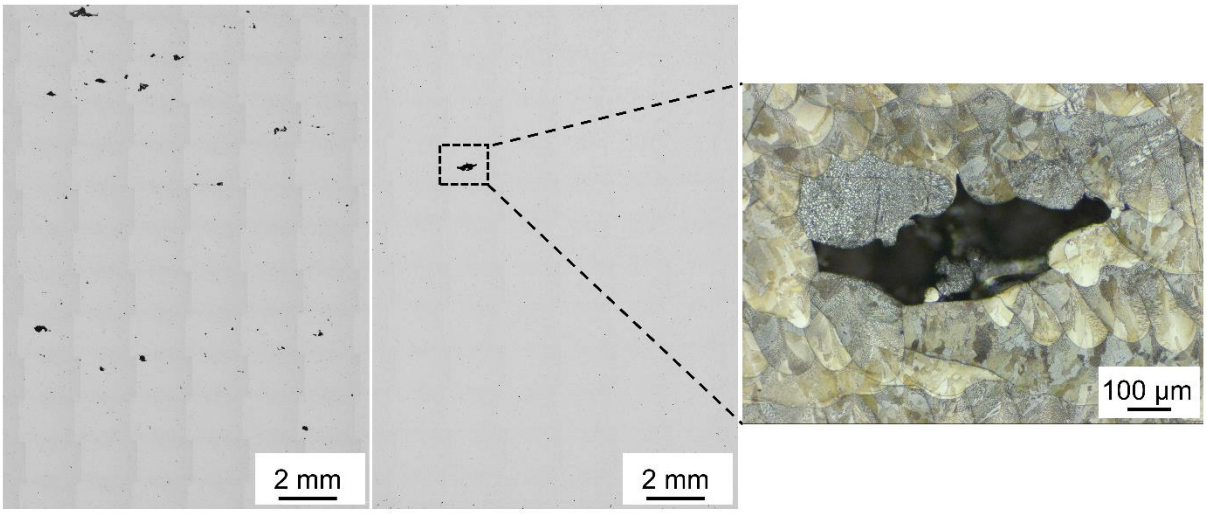

Figure 4 Cross-sections of samples containing stochastic flaws. A higher magnification image of a flaw formed stochastically is also presented.

Spatters are LPBF process by-products whose formation is inherent to the process and have been reported as one of the primary sources of stochastic flaws [27] [25]. Spatters can have varied formation mechanisms and, as a result, different sizes, morphologies and temperatures upon ejection, which affects their detectability. The origins of spatter are schematized in Figure 5. Spatters consist of (**a**) ejections of molten material from the melt pool due to recoil pressure [28], [29], typically with size of 25 – 100 µm [30]. The ejecta can collide and merge (**b**), resulting in even larger particles [30]. Particles entrained by the low-pressure zone created by the vapor jet can interact with the laser beam and be ejected as hot spatters (**c**) [30] or coalesce and be subsequently melted [31], resulting in sizeable incandescent ejecta (**d**). The suddenly unstable interaction between laser and part that arises when the melt pool comes in contact with a pre-existing large flaw can also cause the formation of hot spatter (**e**) [32]. Cold spatters consist of particles initially present on the powder bed that are scattered due to the impact of metallic vapor (**f**) [28] or entrained by the low-pressure zone then directly ejected prior to interaction with the laser beam (**g**) [30].

As a result of their formation mechanisms, spatters can be much larger than the particles in the powder feedstock [33], as illustrated in Figure 6, and contain surface oxides up to several micrometers thick [34]. When redeposited on the powder bed, spatters represent a local increase of layer thickness and a local change in surface chemistry, which can hinder the complete melting of the powder layer [35] and attenuate the laser beam [27], potentially resulting in insufficient melting, that is, in internal flaws that are detrimental to mechanical properties [36].

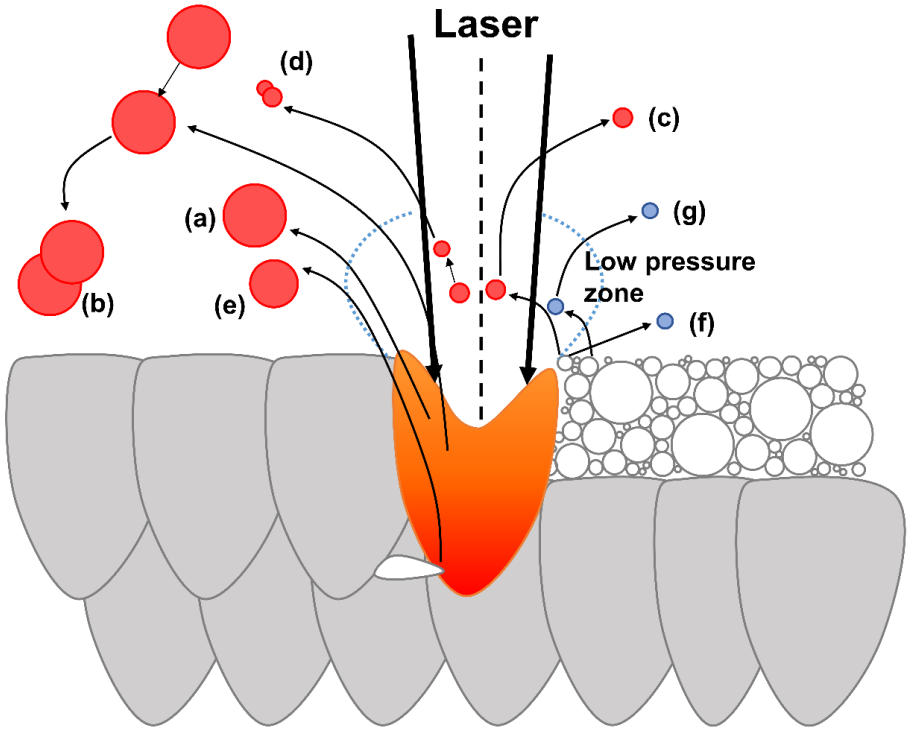

Figure 5 Scheme of spatter formation mechanisms. Spatters can consist of ejections from the melt pool (a), which can also collide and merge (b). The ejection from the melt pool is intensified if the laser interacts with a pre-existing flaw (e). Scattered feedstock powder particles can also be considered spatter and are differentiated by being directly scattered (f), scattered after being entrained in the low pressure zone (g), ejected after interacting with the laser beam (c), or coalesce with another particle (d).

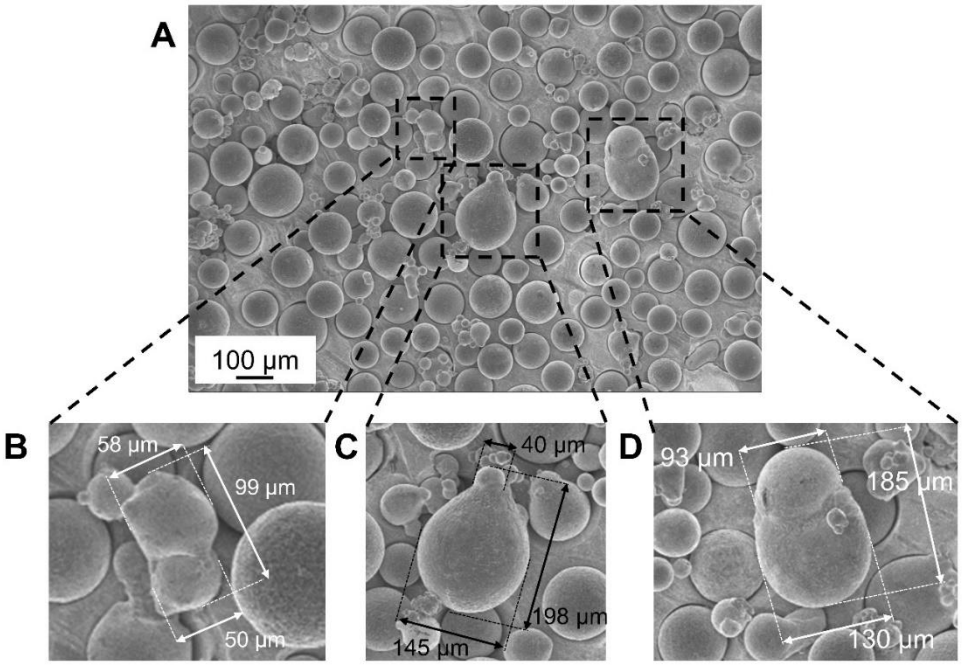

Figure 6 Morphology of spatter particles. A representative sample is shown in A. In B, C and D, some of the oversized agglomerates in this sample are highlighted and measured. From **Paper IV**.

CHAPTER 4
MONITORING ADDITIVE MANUFACTURING PROCESSES

The presence of flaws is inherent to any manufacturing process and is often considered in the design of high-end products [37]. To control the quality of components, as manufactured or in operation, it is crucial to determine whether a flaw is present and, if possible, to estimate its size and location [38]. For this reason, non-destructive inspection techniques, such as radiography and ultrasonic testing, are routinely employed industrially for flaw detection. However, as these methods are typically performed ex-situ and post-manufacturing, they cannot be used to identify or mitigate a flaw upon its formation. Additive manufacturing introduces the possibility to correct flaws during the manufacturing process due to the iterative layerwise nature of the processes. This possibility, together with the need for detecting flaws and the objective of first-time-right manufacturing, originated the great interest in in-situ monitoring and closed-loop control in the additive manufacturing community. The capabilities of various detectors and monitoring setups in various applications, including flaw detection, have been investigated in the literature. As this area of knowledge is relatively new, a literature review will be presented in the next section.

4.1 Literature review

Monitoring systems can be distinguished by the spectral range of the signal acquired and by the acquisition system employed, which can comprise regions of distinct extensions and generate different outputs at varying rates. The selection of acquisition system and spectral ranges determine the process phenomena and deviations that are possible to be captured, as well as the attainable data processing speed. Thus, different monitoring system setups have different best application areas and varying capabilities of being implemented in practice as quality assurance tools.

Optical process monitoring is one of the most common setups for the detection of flaws in LPBF. The setup often consists of a camera that acquires signal in the visible spectrum across the entire build area in a layerwise fashion, after recoating or after laser exposure. This system has been used to identify regions of the powder bed affected by recoating issues, such as recoater streaking and incomplete spreading. Machine learning approaches have been employed to differentiate powder spreading issues [39] as well to distinguish irregularities from the desirable, normal operating conditions [39] [40].

Even though internal flaws often originate from issues other than inhomogeneities on the powder bed, optical systems have also been widely employed on their detection. In this

approach, the in-situ detection is often validated by the ex-situ detection of flaws. Lu et al. [41] followed this procedure by segmenting the regions of the powder bed not entirely covered by powder after recoating and then correlating the segmented area with the area of internal flaws detected through computed tomography (CT) scan. Gobert et al. [42] used images of the powder bed captured in varying light schemes together with CT scan data to implement a binary classification algorithm in which regions are categorized as a flaw or nominal build conditions. Employing a similar experimental setup, Imani et al. [43] tested multiple machine learning algorithms to distinguish process conditions utilized in the manufacturing, given an image of a part. Caggiano et al. [44] employed a convolutional neural network on powder bed images to distinguish low, high and standard energy process conditions.

Process monitoring based on the acquisition of infrared emissions by means of photodiodes has been extensively used for thermal sensing. This detector type is often employed to monitor melt pools in LPBF, as it acquires signal from a small surface area at a time [45]. This device set to detect wavelengths between 780 nm – 900 nm was employed in the monitoring of melt pool intensity [46] and for detection of deformation due to thermal stresses and overheating in overhang structures [47], after translation of the time coordinate to spatial coordinates. In a similar setup but using a distinct detection bandwidth (1150 nm – 1800 nm), photodiodes were used to detect flaws created deliberately through blockage of the gas flow [48], [49]. Using a diode with bandwidth 1500 nm – 1700 nm combined with ex-situ radiography of single tracks, Forien et al. [50] identified signal deviations that corresponded to keyhole pores.

Other monitoring systems that collect high-resolution data are based on high-speed cameras and acoustic emissions, which, due to the large amount of data generated, are often limited to the analysis of single tracks. Machine learning approaches have been applied to classify images acquired through high-speed cameras [21] [51] and acoustic signals [52] into categories based on the quality of single tracks, such as balling, continuous tracks and keyhole porosity. Acoustic emissions could also be applied to determine the quality of a bulk specimen containing sections manufactured at different sets of process parameters, yielding systematic flaws [53].

Cameras can be used to capture signal from the entire build area and, if employed in conjunction with high-pass filters, can be used for thermal sensing. However, reliable temperature measurements can be obtained through the use of specific devices, such as pyrometers, which undergo rigorous and careful calibration prior to being considered a temperature measurement device [57]. Yadroitsev et al. [54] employed A CCD camera to estimate melt pool temperature throughout the process. A thermographic camera with a spectral range of 4800 nm – 5200 nm was employed to identify delamination and spatter [55]. Thermal imaging has been successfully employed in the detection of internal flaws in direct energy deposition. After extracting geometrical features of thermal images of the top surface of melt

pools, Khanzadeh et al. [56] tested multiple models to classify melt pools into normal or abnormal, the latter resulting in internal flaws. The existence and location of the predicted internal flaws were verified through CT scan.

4.2 Process monitoring focused on the detection of flaws

Before monitoring can be used as a quality assurance tool, it is necessary to calibrate the system and qualify the detection procedure in order to ensure a fair correspondence between detections and flaws of interest. In traditional non-destructive inspection methods, flaws of controlled dimensions are created artificially, and the system is calibrated to generate a distinct signal on those locations. Since in AM the goal is to detect flaws while the manufacturing process is ongoing, the method employed in the deliberate creation of flaws becomes an issue to be considered. The intentional creation of internal voids through the inclusion of such features in the geometrical model has been reported in the literature [40][58][59][60]. However, this approach contains limitations as it does not mimic the process of flaw formation and, by basing calibration of the system on those voids, fine features that are usually present in the design of AM parts will be incorrectly detected as flaws. Hence, to calibrate the system, the process of intentionally creating flaws must preserve the physics of flaw formation.

CHAPTER 5
IMAGE ANALYSIS

As the output of one of the monitoring systems employed in this thesis (EOSTATE Exposure OT) are images, image analysis methods are employed aiming to identify flaws. A brief and simplified overview of these methods is presented in this chapter.

A digital image is an array of intensity values. As such, mathematical operations performed in vectors can be applied to images. In a filtering operation, a dot product is performed between the image and a typically small element, also called filter or kernel, thus generating a filtered image as an output. As the filter is smaller than the image, the operation is done in a sliding window manner until all the pixels in the image have undergone the operation, as schematized in Figure 7, in which a sample grayscale image obtained from EOSTATE OT monitoring is represented. The pixel values are in the range $[0, 1]$, where high values correspond to bright areas, and low values correspond to dark areas. A Gaussian filter of dimension 5 x 5 is represented.

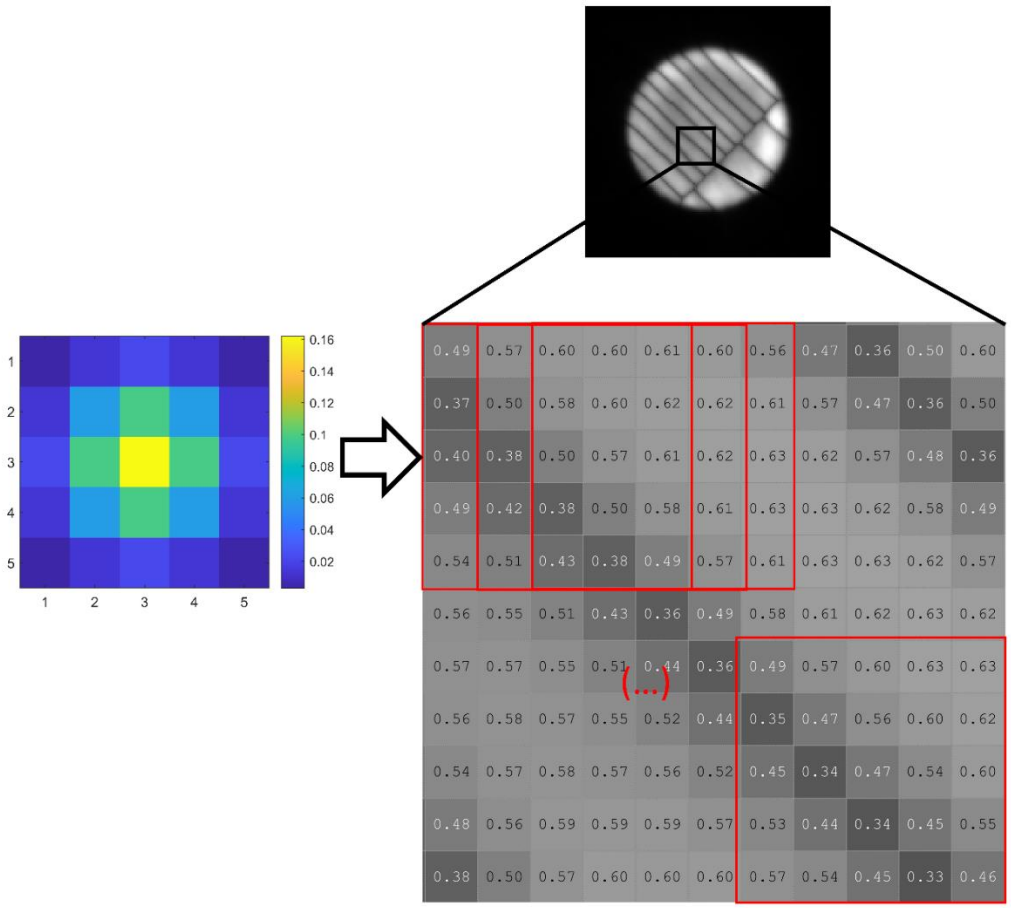

Figure 7 Scheme of a filtering operation. A sample output image acquired through the OT monitoring system and a 5 x 5 Gaussian filter are represented.

Gaussian filtering is one of the most common operations in image analysis. It is frequently employed as a preliminary step to reduce noise and enable the identification of features of interest only. The Gaussian filter is a discretized version of the Gaussian function and can be expressed as:

$$g_\sigma(x,y) = \frac{1}{2\pi\sigma^2}\exp\left(-\frac{x^2+y^2}{2\sigma^2}\right) \quad (1)$$

The standard deviation σ determines the degree of smoothing and allows for observation of the image in different scales (i.e., different levels of detail). The sample monitoring system image is visualized in Figure 8 with increasing degrees of blurring, according to the operation schematized in Figure 7.

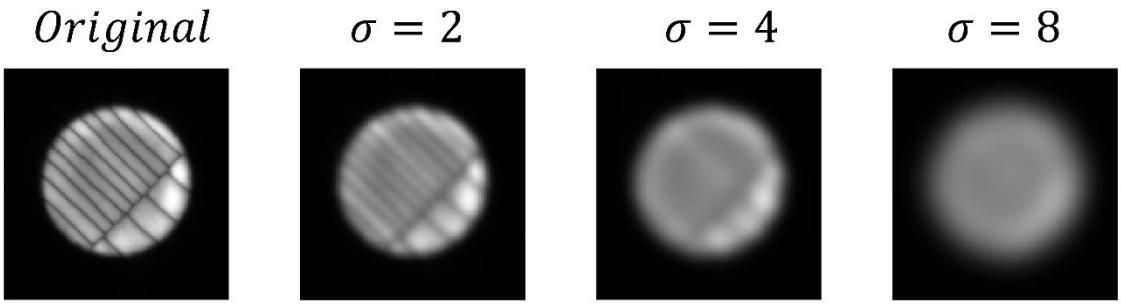

Figure 8 Sample image acquired through the OT monitoring system filtered with a gaussian kernel with distinct standard deviations, generating increased blur.

The gradient at the position (x,y) of an image I is:

$$\nabla I(x,y) = \begin{pmatrix} I_x'(x,y) \\ I_y'(x,y) \end{pmatrix} \quad (2)$$

Similar to Gaussian blurring, in image analysis, the computation of gradients is performed with discrete filters. The derivatives of the sample OT image in x- and y-direction, as well as its gradient, both computed and represented in a plot, can be observed in Figure 9. Such operation outputs a vector on each pixel of I, oriented towards the region of higher intensity. The magnitude of the gradient represents how sharp the intensity changes are. Thus, computation of the gradient is often employed in edge detection, yet another common operation in image analysis.

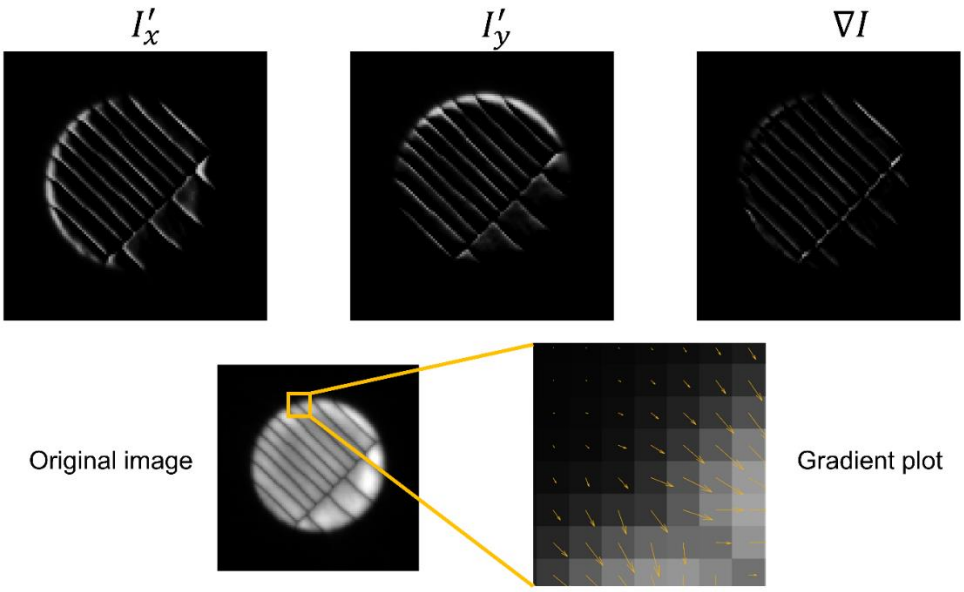

Figure 9 Derivative filters for x- and y-directions applied to a sample OT image. The resulting gradient estimative is both computed and represented in a gradient plot.

The second derivative of an image can be computed to identify blobs, which are, in grayscale images, regions of distinct intensity in relation to the surrounding areas. One of the most common blob detectors is the Laplacian of Gaussian (LoG) operator [61]:

$$\nabla^2 G(x, y, \sigma) = \frac{x^2 + y^2 - 2\sigma^2}{\pi\sigma^4} \exp\left(-\frac{x^2 + y^2}{2\sigma^2}\right) \quad (3)$$

Since the convolution operation is associative, the application of the LoG filter is equivalent to a two-step convolution, in which the Gaussian step attenuates noise, while the Laplacian is a measure of the second derivative of the smoothed image and highlights regions of rapid intensity change. In this operation, the standard deviation determines the size of the features identified. A threshold applied to the convolved image determines the sensitivity. This operation is performed in this thesis in a detection problem, in which the location of the features of interest are the desired output. When applied in a single patch of the original image, the filter can be seen as a classifier, as it will classify the patch as either containing the feature or not. When applied in a sliding window manner, the classifier can be seen as a detector, as it will output the feature locations.

In neural networks, input data are combined to generate the nodes in the next layer. Each node in the next layer is then combined to generate the neurons in the next layer, successively for a number of layers, to finally generate an output, as schematized in Figure 10. In the context of image analysis, neural networks can be applied for classification problems, in which the outputs are pre-defined classes [62]. The combinations of the input data and intermediate layers consist of filtering (or convolution) operations, whose output is passed through a non-linear function

ξ to add discriminative power, as schematized in the insert in Figure 10. One of the most commonly used functions is the Rectified Linear Unit (ReLU), $\xi(x) = \max(x, 0)$.

At the end of a neural network that performs multi-class classification, probabilities are calculated for each pre-defined class through the softmax function, and the class corresponding to the highest probability is the predicted class. The weights w_i in the linear functions are parameters that will be learned by the model. In the context of image analysis, these parameters determine the filters used by the network to extract features that can best represent and distinguish the images from each class. In the first layers, low-level features such as edges and corners are extracted. In deeper layers, the extracted features are increasingly abstract [63]. The learning process starts with the model initializing values to those parameters and attempting to predict the output. As the output has been previously labeled, the model can determine how successful the prediction was based on the parameters initially employed and adjust them. In short, the adjustment is made by firstly computing the loss function, which is the negative log-likelihood of the probabilities calculated by the softmax function. The gradient of the loss function is computed in a process called backpropagation and is minimized by gradient descent. This process is done iteratively in the process of training the network. At each iteration, one test example is randomly chosen. Once all the test data have gone through the process, it can be repeated for as many epochs as necessary. As the training progresses and the model learns parameters in order to minimize the loss function, it is possible that the model overfits to the test data. To prevent that, a validation set is used, in which the loss function must continue to decrease as the training progresses.

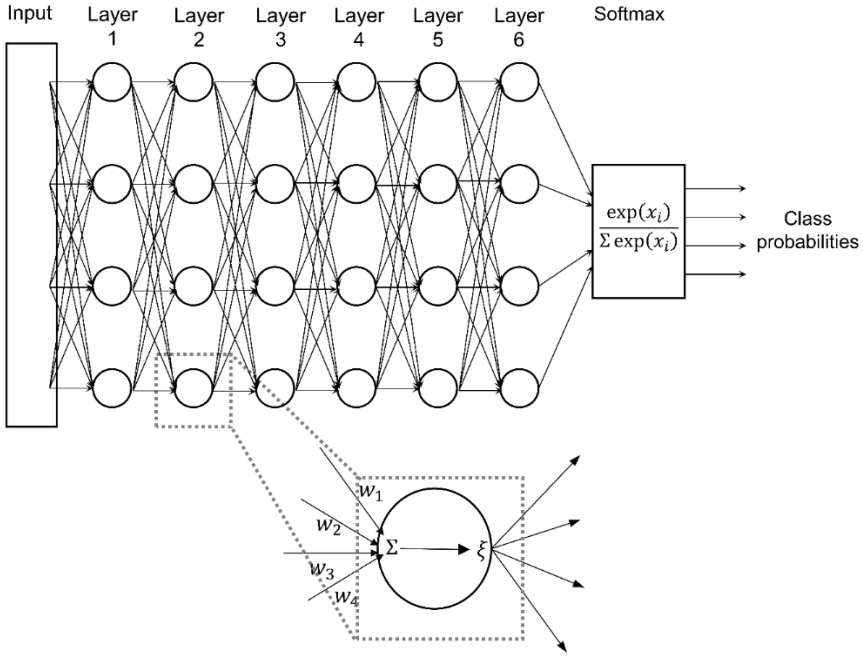

Figure 10 Schematic neural network for a classification problem

CHAPTER 6
HASTELLOY X

Hastelloy X is a nickel-chromium–iron-molybdenum alloy, also referred to as a superalloy due to its excellent resistance to chemical and mechanical degradation at high temperatures over extended periods of time [64]. Nickel is the base element of most heat-resistant superalloys and provides an austenitic structure that has greater formability than ferritic structures of equivalent strength. The addition of chromium increases the strength and oxidation resistance at elevated temperatures, while iron reduces the susceptibility to internal oxidation [65], provides solid solution strengthening and cost reduction. Elements with large atomic radius, such as molybdenum and tungsten, contribute to strength at high-temperature creep, as strength is diffusion dependent in this temperature range [65]. Contrarily to other nickel-based superalloys, Hastelloy X is not enriched with titanium and niobium, which form the strengthening phases gamma prime and gamma double prime. On the other hand, carbide formation occurs, primarily upon heat treatment or service in high temperatures, improving the creep properties due to the preferred location at grain boundaries [64]. As a result, the primary strengthening mechanism in Hastelloy X is solid solution strengthening of the face-centered cubic (FCC) matrix, with a minor influence of carbide precipitation [66].

Hastelloy X is used in petrochemical applications due to its high resistance to stress-corrosion cracking, in components in the combustion zone of gas turbine engines due to its outstanding combination of oxidation resistance and high-temperature strength, and in industrial furnace applications due to its resistance to oxidizing, reducing and neutral atmospheres [67]. Considering the stringent quality requirements of these areas of application, the capability of manufacturing virtually flaw-free Hastelloy X is crucial. For LPBF manufacturing, this capability relies on the implementation of monitoring systems, which justifies this study and material selection.

The microstructure of LPBF manufactured Hastelloy X can be visualized in Figure 11 and consists of the typical hierarchical microstructure of as-printed LPBF material [68]. The temperature gradient promotes the formation of elongated grains that grow epitaxially in the build direction, visible in Figure 11A across melt pool boundaries. Within the grains, cellular microstructure, which consists of high-density dislocation walls [69], is observed (Figure 11C).

Matrix-strengthened nickel-base alloy Hastelloy X is considered to have good weldability [67], which means it is not particularly susceptible to metallurgical cracks. The AM community, however, is not unanimous regarding the formation of cracks during LPBF manufacturing of Hastelloy X. This issue has been reported and addressed in numerous studies, for example [70] [71] [72] [73], while other authors report crack-free material [74] [75] [76]. This inconsistency

is presumably due to minor compositional changes, which are known to influence the susceptibility to cracking [77]. Other factors, such as the grain structure in the fusion zone, can affect the susceptibility to cracking [26]. Throughout the work performed in this thesis, a large portion of the process parameter space was investigated, thereby huge variations in the microstructure were obtained. However, no cracks were observed in any condition, indicating that the specific chemical composition of the feedstock powder used in this study is robust to cracking mechanisms. As no cracks were observed, the internal flaws addressed in this thesis are limited to lack of fusion and pores.

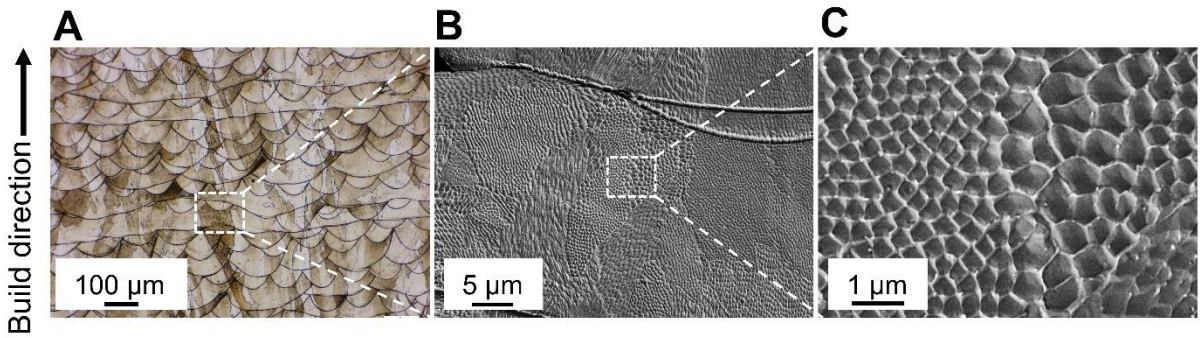

Figure 11 Hierarchical microstructure of as-built Hastelloy X. (A) In the microstructure observed at relatively low magnification through light optical microscopy, grains elongated on the build direction and melt pool boundaries are visible. (B) Through SEM imaging, the cellular microstructure is visible within grains. The well-defined lines are melt pool boundaries. (C) Detail on cell structure. From **Paper III**.

CHAPTER 7
EXPERIMENTAL PROCEDURES

7.1 Material

All the work performed in this thesis used EOS NickelAlloy HX as feedstock material, which consists of gas atomized Hastelloy X powder with particle sizes ranging from 19 µm (d10) and 58 µm (d90), having d50 of 35 µm. A sample of the virgin feedstock powder can be seen in Figure 12. The nominal chemical composition, as provided by the manufacturer, is presented in Table 1.

Table 1 Nominal composition of the feedstock powder. Minimum and maximum weight percentages of each element are presented.

	Ni	Cr	Fe	Mo	W	Co	C	Si	Mn	S	P	B	Se	Cu	Al	Ti
Min	Bal	20.5	17.0	8.0	0.2	0.5	--	--	--	--	--	--	--	--	--	--
Max		23.0	20.0	10.0	1.0	2.5	0.1	1.0	1.0	0.03	0.04	0.01	0.005	0.5	0.5	0.15

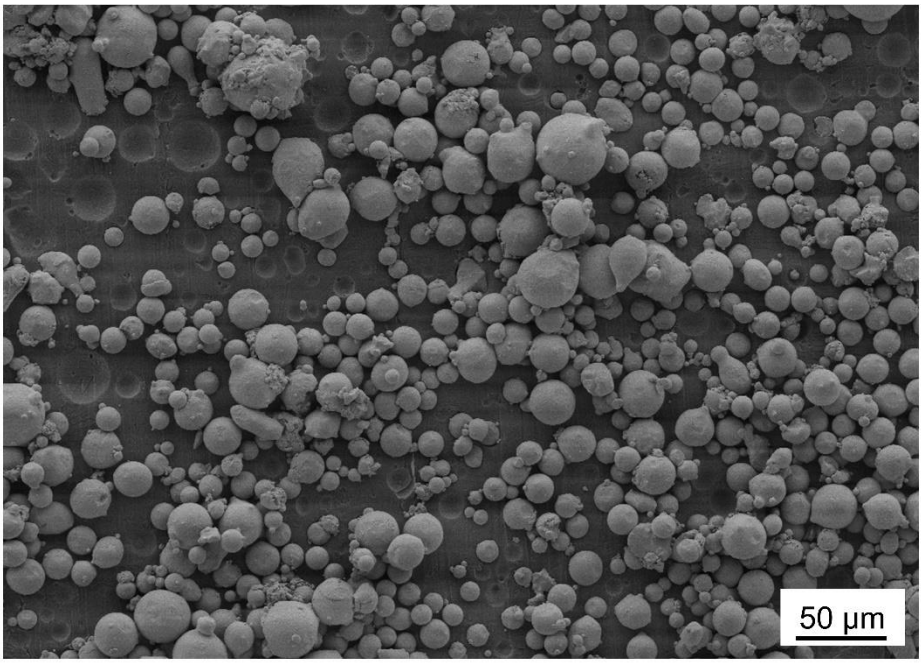

Figure 12 Sample Hastelloy X feedstock powder.

7.2 LPBF system and the manufacturing process

All manufacturing was performed in an EOS M290 machine (Electro Optical Systems GmbH, Germany), equipped with an ytterbium fiber laser of maximum nominal power of 400 W and focused beam diameter of 100 µm. Processing was done in argon atmosphere with oxygen

concentration less than 0.10%. As this work is dedicated to studying internal flaws, it does not consider surface roughness and flaws open to the surface, as well as their mitigation though, e.g., appropriate selection of contour parameters. Additionally, relatively simple specimen geometries were employed to avoid the incorporation of flaws driven by factors such as design and parameters assigned to special areas (*downskin* and *upskin*). In order to eliminate the action of factors other than the study subjects, the general processing conditions were maintained constant as per the machine manufacturer's recommendations, unless explicitly stated otherwise. Examples of such factors are the atmosphere, the differential pressure in the chamber, the preheating temperature of the build plate and the scan strategy.

In the studies where systematic flaws were investigated, some precautions were taken to avoid the formation of stochastic flaws. The specimen dimensions were reduced to avoid redeposition of spatter generated during exposure of the upstream region of the specimen on the downstream region. The specimens were positioned with a minimum separation of 40 mm and avoiding the region of the build plate closest to the gas outlet to prevent redeposition of process by-products on the laser-exposed area. In order to mitigate incomplete spreading of the powder layer, the powder dosing was boosted. To avoid recoating-driven flaws, geometrically complex features were not included in the design.

Conversely, when studying stochastic flaws, the source of systematic flaws was eliminated, i.e., the process parameters employed are optimized and had been demonstrated to yield only residual porosity as flaws in the as-printed condition. Still, to isolate the influence of process by-products on the formation of stochastic flaws, the same precautions were taken to eliminate other possible sources of stochastic flaws.

7.3 Monitoring systems

The manufacturing process was monitored utilizing the EOSTATE suite [78], which consists of three monitoring systems. EOSTATE PowderBed is an optical monitoring system that includes the entire powder bed in the field of view of the camera and outputs two images of the powder bed per layer, one after recoating and one after exposure. EOSTATE Exposure OT system consists of a 5-megapixel sCMOS (scientific complementary metal-oxide-semiconductor) camera positioned on top of the build chamber and covers the entire build platform area in its field of view. A bandpass filter of 900 nm ± 12.5 nm is placed on the camera to filter detection of reflected laser, plasma radiation and visible light, regarded as environmental noise. During the processing of a layer, images are acquired sequentially, with the shutter time of the camera set to 0.1 second. These images are combined in two distinct manners to output a single image per layer: each pixel in the output image either represents the maximum pixel intensity or the integrated pixel intensity the exposure of the layer. The resolution is 125 µm per pixel. EOSTATE MeltPool monitoring consists of two photodiodes, one mounted on-axis and one mounted off-axis. The photodiode mounted on-axis, that is,

coaxially with the laser beam, has a bandwidth inserted in the visible and near-infrared spectra, while the photodiode mounted off-axis has a narrower bandwidth that only includes a fraction of the near-infrared spectrum. The signals are initially acquired in the time domain at 60 kHz but are also translated to spatial coordinates, allowing enhanced data visualization. Sample outputs of all three systems are shown in Figure 13. In this thesis, only EOSTATE Exposure OT and EOSTATE MeltPool were utilized.

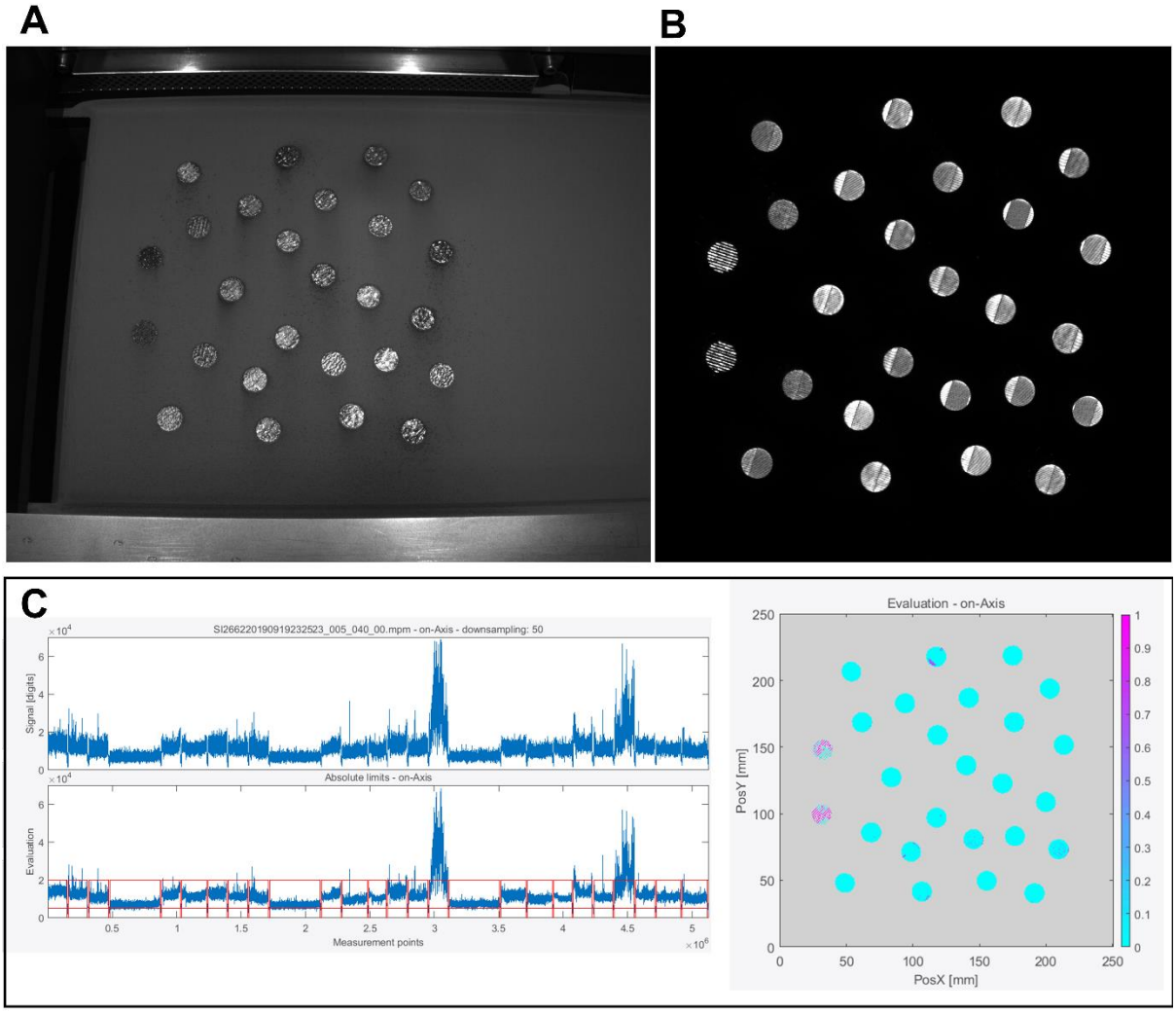

Figure 13 Sample outputs of EOSTATE monitoring systems. (A) Powder bed monitoring after laser exposure. (B) Image acquired through Exposure OT. (C) The output of melt pool monitoring consists of temporal signal intensity (upper left panel) but can be translated to spatial coordinates (right panel). Application of signal processing discriminates regions containing anomalies (lower left panel), which are also highlighted in the spatial representation.

7.4 Analytical techniques

Metallography

All specimens prepared for metallographic analysis were sectioned in the same fashion: parallel to the build direction and transversally to the topmost scanning tracks. Specimen preparation was conducted by standard metallographic procedures, namely plane grinding with 320-grit

sandpaper, followed by fine grinding with 9 µm diamond suspension on a Struers MD-Largo surface and finally colloidal silica polishing. Electrolytic etching was performed in a solution of 5 g oxalic acid mixed with 95 ml reagent grade HCl at 6 V.

Specimens in which quantification and measurement of internal flaws were conducted had a relatively large cross-section of 10 mm x 20 mm, approximately. Each of those cross-sections was fully imaged in the unetched condition using the stitching tool in Zeiss Axioscope 7 light optical microscope at 50x magnification, yielding detectable features down to 0.88 µm, the size of a pixel. The resulting images were processed by an image analysis algorithm that returns the properties of each contiguous region in the binarized image. Among the quantities measured are the flaw length, also referred to as flaw size, as well as area fraction of flaws, referred to as volume fraction of flaws, assuming that the area is representative of the bulk.

The flaw size distribution is typically a right-skewed distribution, with a high quantity of small flaws and a low number of larger flaws, as illustrated in the histogram in Figure 14. Since larger flaws are more detrimental to mechanical properties [37] [79], a representation of flaw size distribution that highlights larger flaws is preferred and achieved in the form of curves representing the cumulative flaw content against flaw size. In this graphical representation, the total volume fraction of flaws (100 – relative density, in %) can also be clearly visualized.

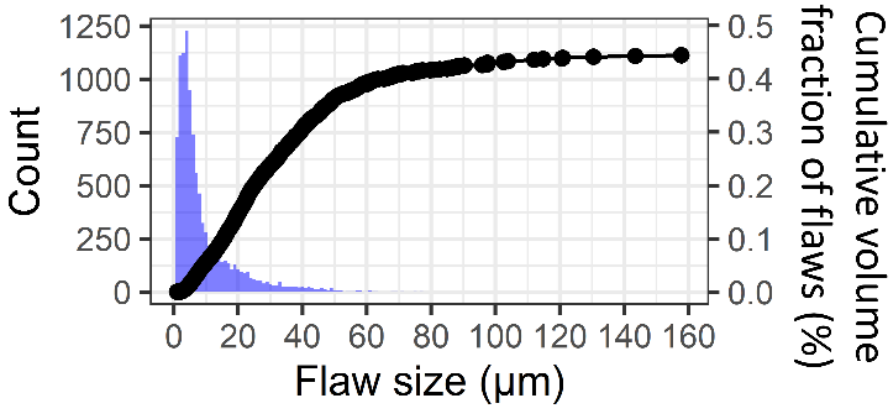

Figure 14: Alternative representations of flaw size distribution.

Scanning electron microscopy

In scanning electron microscopy (SEM), a focused electron beam is used to scan the surface and near-surface of the specimens under analysis. The interaction between the electron beam and the material under observation generates different signals, among which secondary electrons and backscattered electrons, used for imaging, and X-rays, used for chemical analysis.

The SEM work done in this thesis employed a field emission gun scanning electron microscope (FEG-SEM) Leo Gemini 1550. SEM was used for microstructural characterization of the as-printed Hastelloy X, analysis of fracture surfaces, and characterization of powder and spatters

in terms of morphology and surface morphology. The latter experimental work was conducted by Ahmad Raza.

Electron backscatter diffraction (EBSD) is a technique integrated into SEM systems that provides data on the crystallography of materials, for example, grain size, shape and orientation, and allows the identification of phases and texture. The EBSD analysis was conducted by Dr. Fiona Schulz.

Ultrasonic inspection

Ultrasonic inspection is a mature technology widely used in industry to detect flaws. In this thesis, its output was compared to the overall distribution of internal flaws detected through the monitoring system.

The ultrasonic inspection was performed in the form of a linear scan transversally to the build direction, with a 64-elements linear phased array longitudinal-wave-probe (Zetec LM-5MHz), fixed at a single position on each specimen analyzed. The ultrasonic waves were emitted from an aperture of 16 elements of the probe and propagated into the specimen with a 0-degree refraction angle. Proper delay laws were applied to realize the beam focusing at one scan position. In order to cover the entire region of each build, the aperture travels along the whole array with a step of 1 element. The ultrasonic inspection data were collected and recorded under a sampling frequency of 100 MHz by a corresponding data acquisition hardware unit labeled TOPAZ64 from Zetec and then post-possessed using UltraVision software. The longitudinal wave speed in Hastelloy X is about 5700 m/s. Using the phased array probe with center frequency of 5 MHz, the wavelength in this material is about 1.1 mm, which allows for the detection of flaws larger than 500 μm [22]. The ultrasonic testing was conducted by Xiangyu Lei.

X-ray photoelectron spectroscopy

X-ray photoelectron spectroscopy (XPS) is a surface analysis technique that has been utilized in this thesis to identify the chemical state of the elements present on the surface of powder and spatter particles. Powder samples were mounted on 3M carbon tape and analyzed using a PHI VersaProbe III Scanning XPS microprobe (Physical Electronics, Inc.). To estimate oxide layer thickness on the surface of the samples, argon ion etching was done with etch rate of 5.2 nm/min, calibrated using TaO_2 foil. The etch rate was assumed to depict the rate of etching of transition metal oxides [80], and a method specifically developed for XPS depth-profiling of powdered samples was employed [81]. The survey spectra and high-resolution narrow scans were acquired using pass energies of 280 eV and 26 eV, respectively. The XPS analysis was conducted by Ahmad Raza.

Signal processing and image analysis

The signal acquired through melt pool monitoring (EOSTATE MPM) was processed according to two distinct algorithms. The signal intensity characteristics were calculated as the moving average in windows comprising 600 data points, while the signal dynamic characteristics were computed as the raw signal minus the moving average to highlight dynamic process changes.

Image analysis methods are employed in the output of EOSTATE Exposure OT. All data handling and image analysis is performed in a Matlab R2019b environment. One of the problems that can be handled through image analysis is classification, in which a classifier takes an input image and outputs an appropriate label. In the study of systematic flaws, a convolutional neural network was used to classify images acquired through in-situ monitoring into three categories of internal flaws, whose presence was verified ex-situ through metallographic analysis. In this approach, a significant number of labeled examples is provided to a model that learns the optimized parameters to output the correct label. The labeled examples are partitioned into three sets: the training set, used to fit the parameters in the network; the validation set, which provides an evaluation of the model during the training process and prevents overfitting; and the test set, set apart in previous stages for the evaluation of the final model.

In the study of stochastic flaws, image analysis was framed as a detection problem. The redeposited spatters manifest as bright blobs on a darker background, and their detection can be treated accordingly. For that, a Laplacian of Gaussian (LoG) filter is utilized. The standard deviation σ is selected so the filtered image converges to local extrema upon detection of a spatter redeposit. Due to the homogeneous size of the features (~100 µm) in relation to the camera resolution (~ 125 µm), detections were performed at a single scale. After filtering, non-minimum suppression, a filtering technique that returns true to the pixel that has a strictly lower value than its neighboring pixels, was applied to ensure unique detections in each spatter.

CHAPTER 8
SUMMARY OF RESULTS

This chapter summarizes the results of the appended papers. **Papers I**, **II** and **III** address systematic flaws. In **Paper I**, the flaw populations and melt pool geometries were mapped in the process parameter space. The capabilities of the melt pool monitoring system of predicting melt pool geometry, melt pool dynamics, and internal flaws were then evaluated. In **Paper II**, the data collected ex-situ in **Paper I** were used to classify the images acquired through the OT monitoring system into the predominant flaw type encountered in the specimens. In **Paper III**, the virtually flaw-free region of the process parameter space identified in **Paper I** was studied in detail to assess the variation of microstructure and properties in a productivity-focused perspective. Finally, **Paper IV** addresses the formation and detection of stochastic flaws caused by the deposition of spatters on the powder bed.

8.1 Systematic flaws

In **Paper I**, a full factorial design of experiments was employed on the manufacturing of Hastelloy X specimens, with factor levels selected to comprise a vast portion of the process parameter space. In-situ monitoring of the melt pool was performed throughout the entire manufacturing process. Ex-situ measurement of the melt pool widths and depths and analysis of the internal flaws were conducted at each experimental point. The volume fraction of flaws at each experimental point can be seen in Table 2, in which the transition between keyhole and conduction is represented with a dashed line.

Table 2 Volume fraction of flaws (%) across the process parameter space. Laser power, scan speed and layer thickness are varied systematically. The dashed lines indicate the location of transition between keyhole and conduction fusion. "N/A" indicates manufacturing could not be completed due to extreme processing conditions. The highlighted cells correspond to process conditions considered desirable. From **Papers I / III**.

			Laser scan speed (mm/s)							
			200	**400**	**600**	**800**	**1000**	**1200**	**1400**	**1600**
Laser power: 100 W	**Nominal layer thickness (µm)**	**20**	0.39	0.01	0.31	1.41	5.48	7.97	11.6	14.2
		40	0.14	0.76	0.78	5.95	14.3	19.4	27.3	32.1
		80	5.61	11.7	16.5	26.8	35.1	45.4	N/A	N/A
Laser power: 200 W	**Nominal layer thickness (µm)**	**20**	4.47	2.55	0.03	0.01	<0.01	0.19	0.63	1.27
		40	5.12	2.77	0.02	0.01	0.09	0.44	1.67	4.51
		80	6.79	2.19	0.11	0.31	6.90	12.1	18.8	25.6
Laser power: 300 W	**Nominal layer thickness (µm)**	**20**	N/A	2.34	0.44	<0.01	<0.01	0.02	0.10	0.14
		40	3.31	3.50	0.30	<0.01	0.01	0.04	0.12	0.26
		80	4.50	3.19	0.35	0.01	0.03	0.06	0.39	2.53

Melt pool geometry, signal and internal flaws were analyzed, varying one parameter at a time and separately for keyhole (Figure 15) and conduction regimes (Figure 16). In the examples illustrated in these figures, the laser power is the only process parameter altered. This factor-by-factor analysis revealed that the signals acquired through melt pool monitoring have intensities proportional to average melt pool dimensions and present more important dynamic characteristics following process conditions that increase the generation of spatter, that is, increase in the energy input. Higher scatter in melt pool dimensions is consistently observed in specimens containing higher volume fraction of flaws. The more significant variation in melt pool dimensions is attributed to an increasingly irregular substrate where the melt pools will be deposited, due to the presence of larger and more abundant internal flaws. However, the scatter in melt pool dimensions or the deliberately created internal systematic flaws could not be detected by melt pool monitoring.

Hence, the capability of the OT Exposure system to detect systematic internal flaws was studied in **Paper II**. The images output from the monitoring system were used in a supervised machine learning algorithm, in which the data is labeled according to the predominant flaw types identified in each specimen.

The layerwise acquired images were divided into regions of constant size centered in each specimen and including data from a single specimen in each patch. All patches corresponding to the same specimen received the same label, as the flaws are generated systematically due to the selection of process parameters, and each layer is assumed to be representative of the resulting flaw distribution. The labeled images form a database used for training, validating and testing a neural network.

A fully convolutional neural network was designed to classify images per the main flaw type identified through metallographic analysis. This type of network was selected because it can process inputs of any dimensions, despite the training being performed on images of fixed size, as is the case since the manufactured specimens are geometrically identical. The network layers were designed to handle 81x81 inputs and reduce their dimensions gradually through convolution and max-pooling operations, followed by a final convolutional layer that results in an output of dimensions 1x1x3. This layer is then used as an input to the softmax layer, which calculates the probabilities for each possible class. Finally, a classification layer is used to output a predicted class, "keyhole porosity", "lack of fusion" or "residual porosity".

The validation accuracy of the network is 97.99%. In order to estimate the performance of the network in practice, it was applied to the test set, which consists of 1,122 images previously set apart for this purpose. The performance is described by the confusion matrix presented in Figure 17, which shows the overall accuracy in the test set (97.8%), as well as precision, false discovery rate, recall, and false-negative rate for each category.

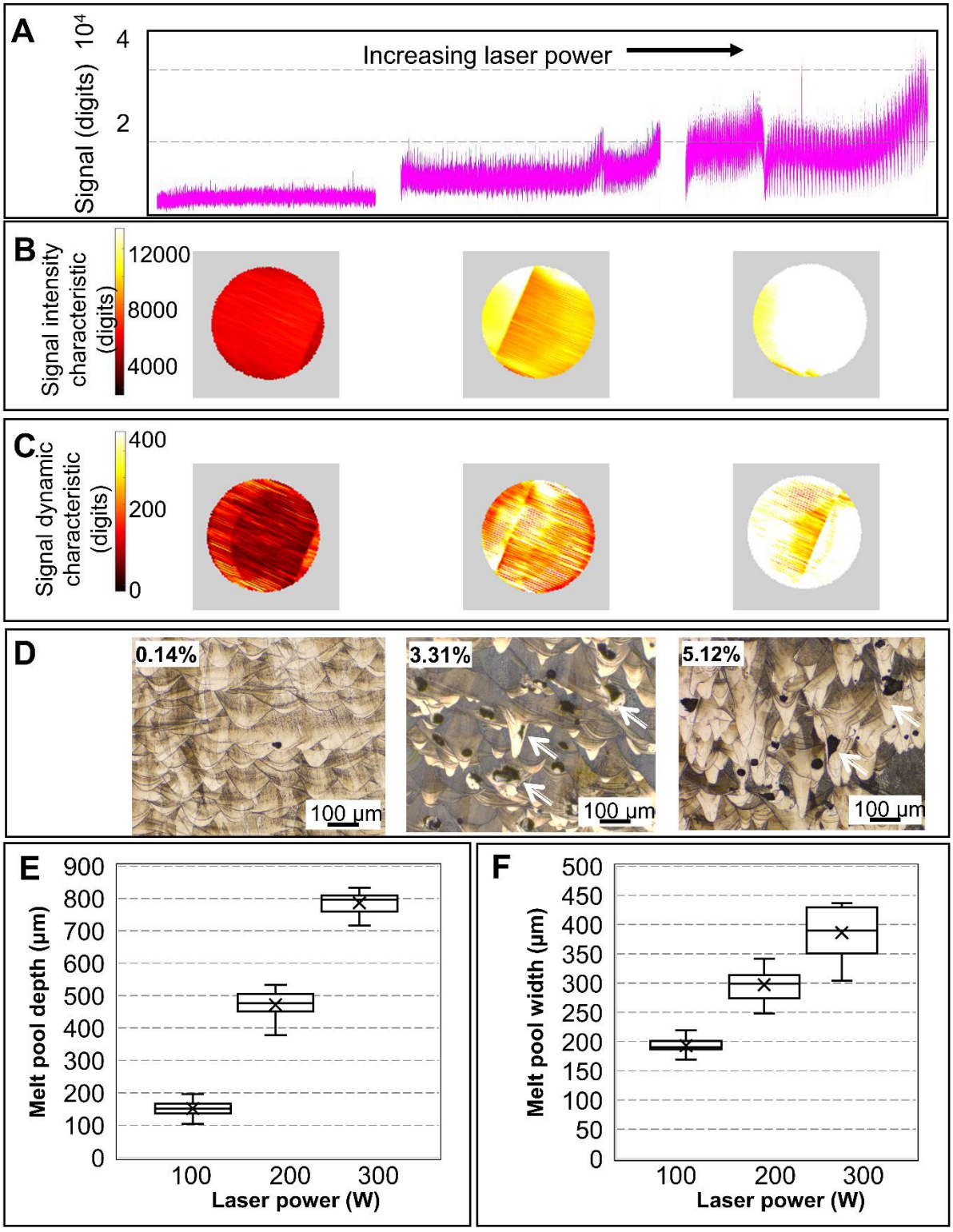

Figure 15 Influence of laser power on melt pool signal characteristics, melt pool dimensions and flaw populations in the keyhole regime. (A) Raw signal in temporal x-coordinate. (B) Signal smoothed and translated to spatial coordinates. (C) Signal processed to highlight regions of high melt pool dynamics. (D) Microstructure of specimens manufactured with laser power 100 W, 200 W and 300 W, and otherwise identical parameters. The volume fraction of flaws is indicated. Influence of laser power on melt pool depths (E), widths (F). Adapted from **Paper I**.

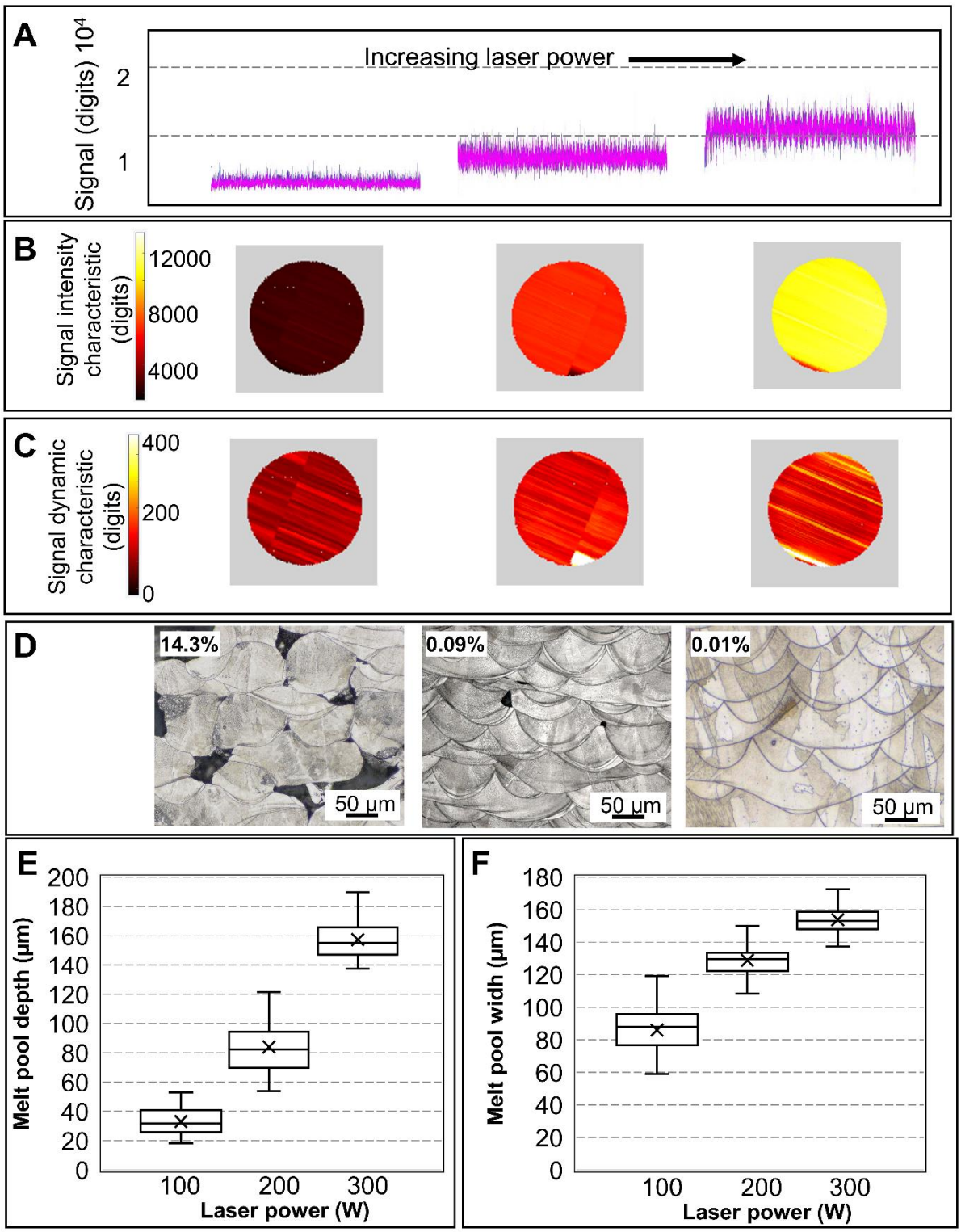

Figure 16 Influence of laser power on melt pool signal characteristics, melt pool dimensions and flaw populations in the conduction regime. (A) Raw signal in temporal x-coordinate. (B) Signal smoothed and translated to spatial coordinates. (C) Signal processed to highlight regions of high melt pool dynamics. (D) Microstructure of specimens manufactured with laser power 100 W, 200 W and 300 W, and otherwise identical parameters. The volume fraction of flaws is indicated. Influence of laser power on melt pool depths (E), widths (F). Adapted from **Paper I**.

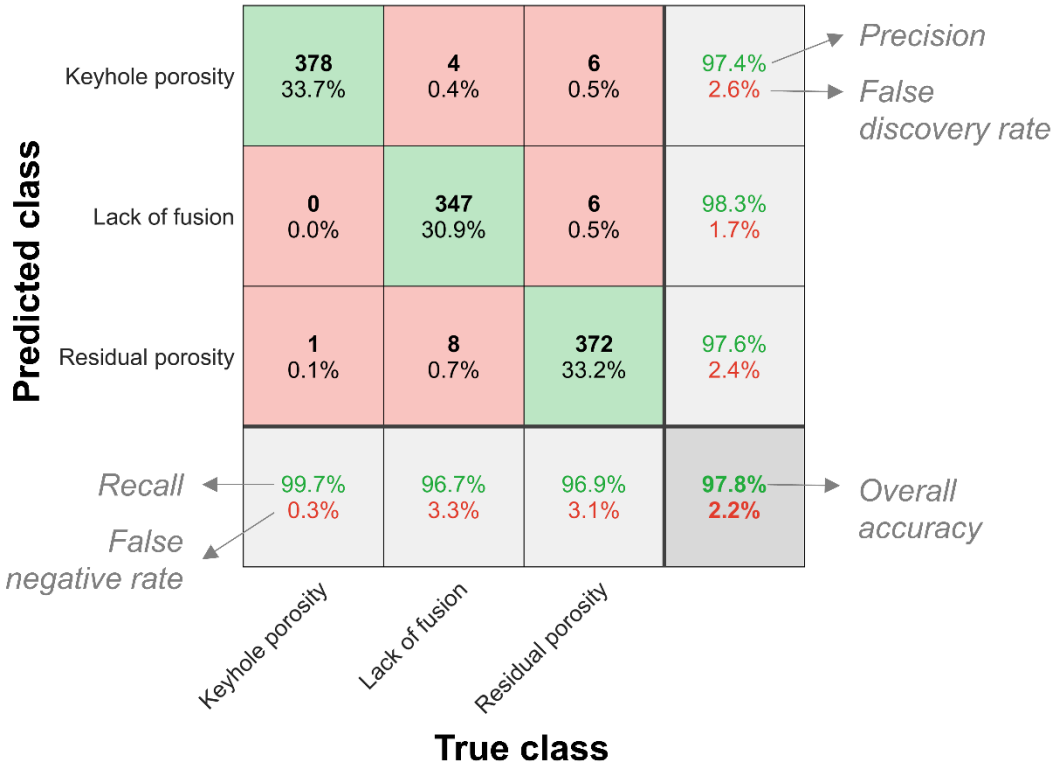

Figure 17 Confusion matrix showing the performance of the network in classifying the 1,122 images in the test set. From **Paper II**.

With that, the amount, type and size of process parameter-driven flaws were characterized for Hastelloy X, and their detectability was ensured. As follows, multiple processing conditions that result in virtually flaw-free material were identified (highlighted in Table 2). These are considered the "desirable" process conditions, as flaw avoidance is achieved through their employment. However, within the range of desirable processing conditions, variability in microstructure, possible properties and achievable build rates are expected. These factors are investigated in **Paper III**, from a productivity perspective.

Considering the absence of a unified approach for the increase of the build rates based on process parameters, the first goal of **Paper III** was to obtain a simplified parametrization of the build rate. For that, it was assumed that the build time is mainly governed by exposure of the bulk region and that the infill parameters and transition time between layers are invariable throughout a build. With that, the build rate can be expressed as:

$$B = \frac{Rvht}{R + \Delta\tau_{tr} vh} \tag{4}$$

Where v is the laser scan speed, h is the hatch spacing, t is the layer thickness, $\Delta\tau_{tr}$ is the time interval for the transition between layers, and R is the average utilization of the build area, which can also be expressed as the ratio between build volume and build height.

Plugging the processing conditions highlighted in Table 2 into Equation (4), the build rates attainable when still producing virtually flaw-free material were obtained. The results are visualized in Figure 18.

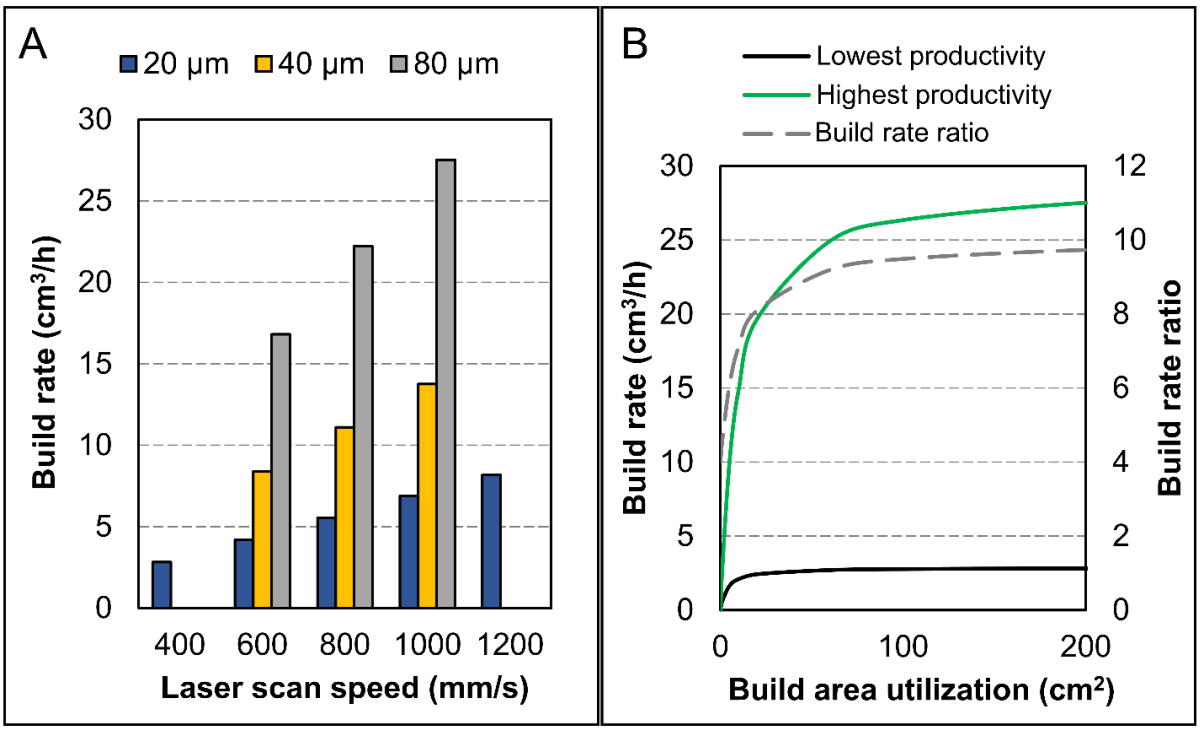

Figure 18 Build rates (cm^3/h) for the sets of process parameters in the process window. The average utilization of the build area is assumed 200 cm^2 in (A). (B) Build rate as a function of the build area utilization for the sets of parameters that enable highest and lowest productivities. The build rate ratio between these sets of parameters is represented by the dashed line. From **Paper III**.

To determine whether an increase in productivity can be achieved without compromising quality, the microstructures of those specimens were analyzed. As multiple process parameters were varied to increase productivity, some microstructural features are expected to vary within the defined process window. The EBSD orientation maps obtained from the specimen produced with the lowest and highest build rates, as well as the influence of each process parameter in the microstructure, are illustrated in Figure 19.

The material produced with the highest productivity (Figure 19b) presents the most random grain orientation and pockets of fine grains at the bottom of the melt pools. Any parametrical change that results in the increase of the energy input to the material promotes grain growth and a stronger ⟨101⟩ orientation of the larger grains. The decrease in layer thickness yields the most significant difference in terms of grain orientation and morphology, as the grains become substantially larger, presenting pronounced elongation in the build direction and strong ⟨101⟩ orientation (Figure 19d).

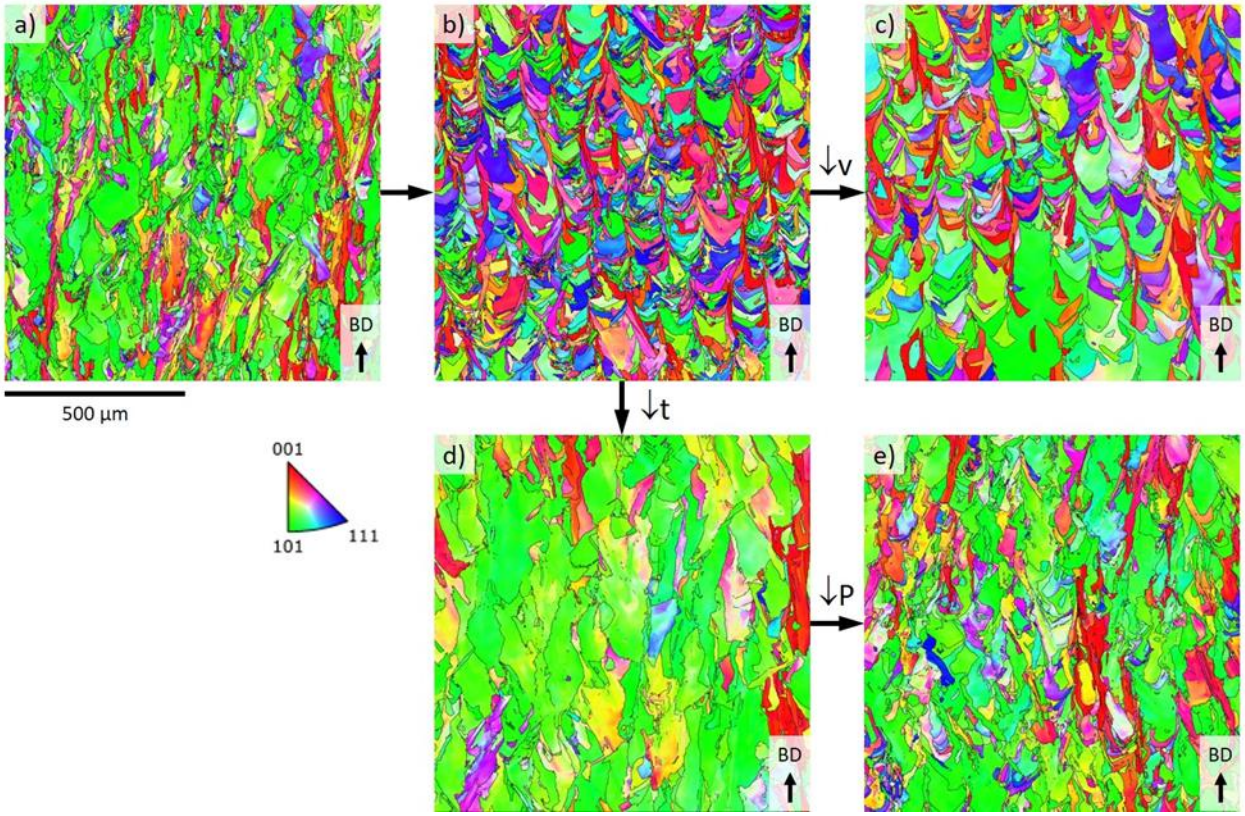

Figure 19 EBSD orientation maps in IPF coloring for material manufactured with a) lowest productivity (specimen #1 – P=100 W, v=400 mm/s, t=0.02 mm), b) highest productivity (specimen #2 - P=300 W, v=1000 mm/s, t=0.08 mm), c) decreased laser scan speed (specimen #3 - P=300 W, v=800 mm/s, t=0.08 mm), d) decreased layer thickness (specimen #4 - P=300 W, v=1000 mm/s, t=0.02 mm), and e) lowered laser power (specimen #5 - P=200 W, v=1000 mm/s, t=0.02 mm). From **Paper III**.

8.2 Stochastic flaws

Spatters can generate internal flaws after landing on the regions of the powder bed to be exposed by the laser beam. Due to the stochastic nature of spatter-induced flaws, in-situ detection of spatter redeposits is paramount, both in a research perspective, for further understanding of spatter behavior, and in a production perspective, for monitoring deviations that indicate flaw formation. In **Paper IV,** three LPBF builds in Hastelloy X were performed with parameters optimized to yield nominally fully dense materials at three distinct layer thicknesses 80 µm, 120 µm and 150 µm. The entire build processes were monitored by EOS OT Exposure, which consists of near-infrared long-exposure imaging and outputs an image per layer. Analysis of these images allowed detection of redeposited spatters, i.e., quantification and determination of their spatial distribution. It was found that the nominal layer thickness employed in the build process plays a major role in the prevalence and distribution of redeposited spatters. Spatters were verified to redeposit preferentially in the adjacencies of the gas outlet; however, as the layer thickness increases, a larger number of redeposited spatters were detected and across a larger portion of the build area, as illustrated in Figure 20. This result represents a major limitation on the increase of LPBF productivity.

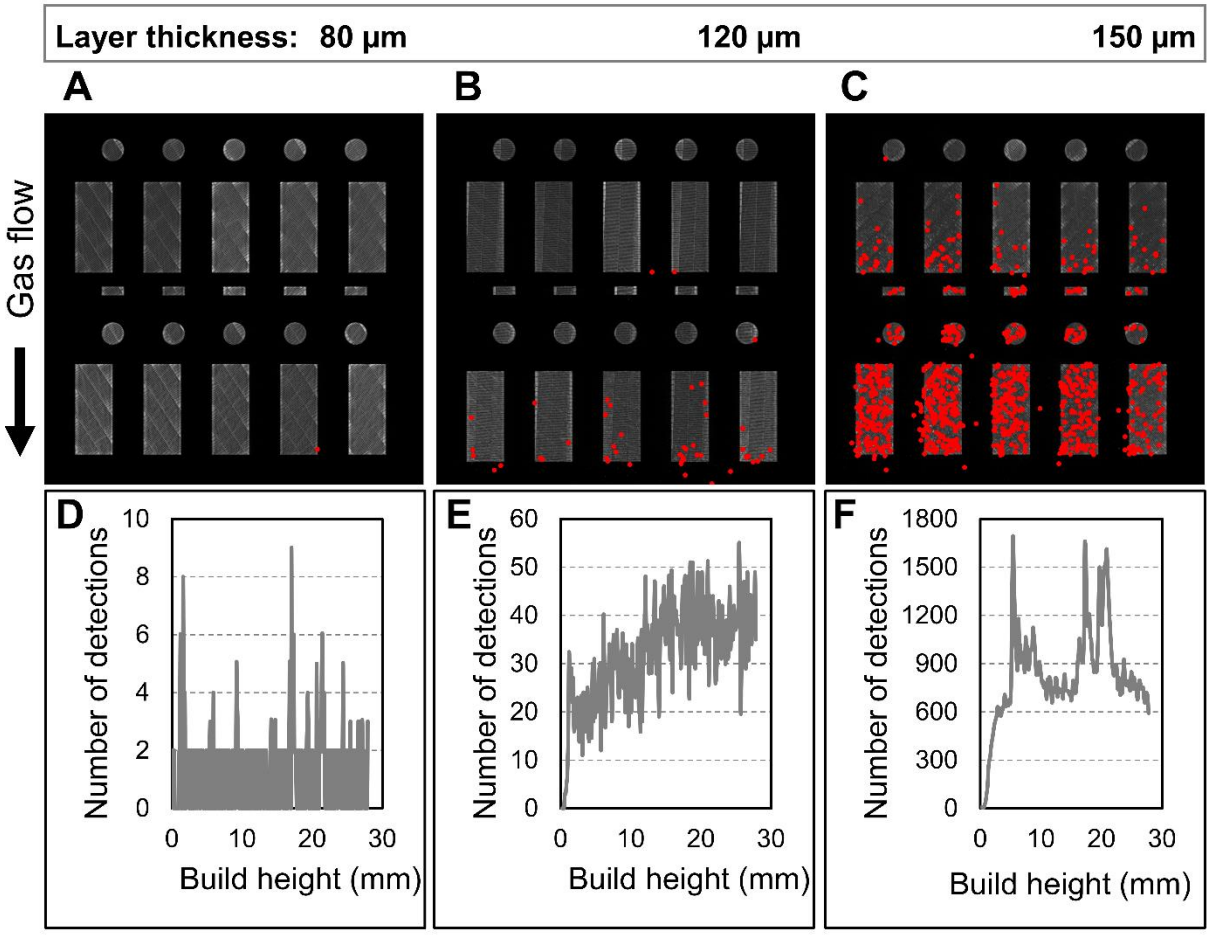

Figure 20 Incidence of redeposited spatters in builds with varying layer thicknesses. Sample detections on builds with layer thickness 80 µm (A), 120 µm (B) and 150 µm (C). The number of detections per layer versus build height is presented in D – F. From **Paper IV**.

The spatter particles collected from the three builds were covered with chromium- and titanium-rich oxide layer of average thickness 76 nm and presented bimodal size distribution with maxima located around 30 µm and 90 µm. No significant differences were observed among spatters stemming from the different builds, which indicated that the striking increase in detections in Figure 20 is mainly due to increased spatter generation with increased layer thickness.

To determine the correlation between detected redeposited spatter and internal flaws, destructive and non-destructive testing were utilized. Both analyses revealed that specimens with a low prevalence of spatter redeposits contain no major internal flaws, and that regions with substantial amounts of detections via in-situ monitoring present lack of fusion, as illustrated in Figure 21.

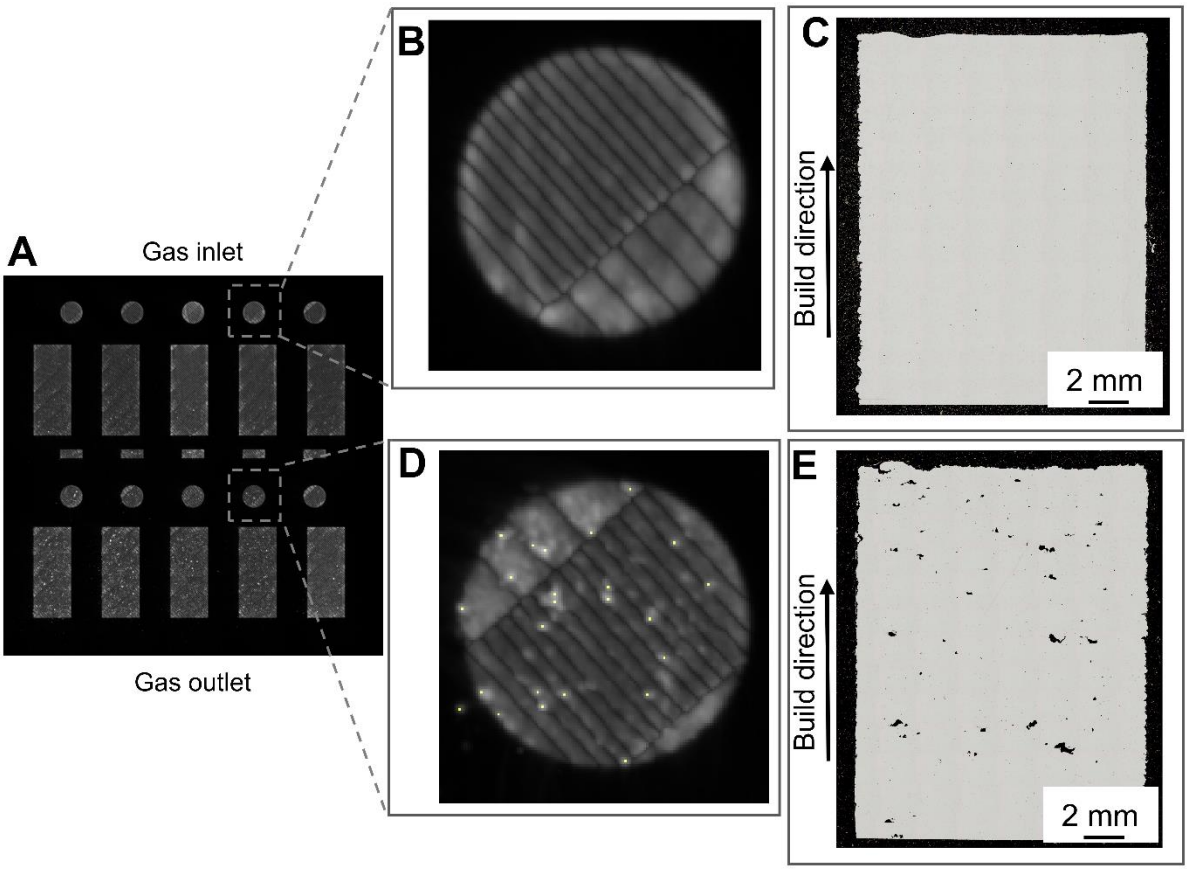

Figure 21 Correspondence between detections of spatter redeposits and internal flaws. Considering the build layout (A), a low number of spatter redeposits are detected in specimens manufactured in the proximity of the gas inlet (B). Metallographic analysis of these specimens reveals no major internal flaws (C). Detections of spatter redeposits can be abundant in specimens manufactured in the proximity of the gas outlet (D), and these specimens present large internal flaws (E). Adapted from **Paper IV**.

Imaging of the cross-section of specimens revealed rounded particles with dendritic structure and often with diameters significantly larger than the feedstock powder in the adjacencies of lack of fusion (Figure 22A), which is evidence that spatter is involved in the formation of these flaws. To confirm that the particles are spatter, analysis of the fracture surface was performed (Figure 22B). The particles located near lack of fusion sites presented the same oxidation state as the spatter analyzed separately, confirming the influence of spatter on the formation of lack of fusion.

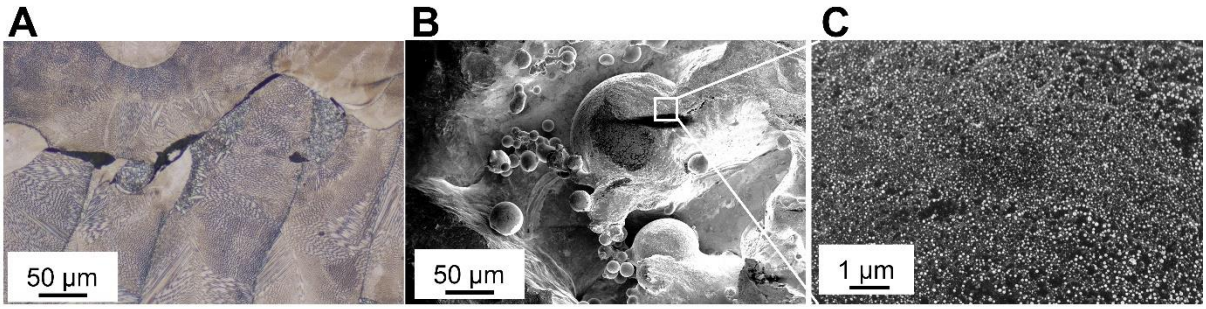

Figure 22 Cross-section of a lack of fusion region (A). Fractography micrograph in lack of fusion of zone (B) with high magnification insert of unfused particle surface (C). Adapted from **Paper IV**.

CHAPTER 9
CONCLUSIONS

This thesis has addressed the classification and detection of internal flaws in LPBF manufactured Hastelloy X, as well as their correlation with melt pool characteristics through the application of in-situ monitoring and ex-situ material characterization. The deliberate creation of flaws was performed according to two distinct approaches that preserve the mechanisms of flaw formation in realistic manufacturing settings. Flaws were created systematically in an extensive process mapping, and stochastically by boosting the amount of process by-products, while the entire build processes were monitored by two systems. The signal acquired through the monitoring systems was processed to identify deviations that could be coupled to flaws and to melt pool features characterized ex-situ. The process mapping also set the basis for process-optimized productivity increase without conflicting manufacturing quality.

Knowing that flaws can be created throughout the material by modifying process parameters, a comprehensive design of experiments was performed with the factors laser power, scan speed and layer thickness, resulting in 72 processing conditions. The flaws in each of these conditions were analyzed qualitatively to classify each processing condition as a generator of a main flaw type, and quantitatively to assess the extension and size of these flaws. This characterization work could then be used not only to identify desirable processing conditions but also to establish ground-truth data for evaluation of the inferences performed through analysis of the monitoring systems outputs (RQ1).

Hence, desirable process conditions based on the incidence of flaws are mapped throughout the process parameter space. After parametrization of the LPBF build rate based on key process parameters and utilization of the build area, it was possible to verify ranges of build rates attainable while avoiding flaws, and to determine strategies for minimization of the total build time. To further determine variability within the preliminarily defined process window, EBSD analysis was performed, revealing striking differences in grain structures. The specimen produced at the lowest build rate showed strong texture and elongated grains along the build direction, while the specimen manufactured at the highest build rate presented random grain orientation and evident melt pool contours with fine grains at the bottom. As productivity increase between these extremes was achieved through the modification of multiple process parameters, the influence of the individual parameters was investigated further. It was observed that pronounced $\langle 101 \rangle$ orientation is consistently obtained when higher energy is input to the material, as larger regions are then remelted, and the competitive growth in this direction is enhanced (RQ4).

From monitoring the melt pool by means of a photodiode with bandwidth 450 nm – 850 nm mounted on-axis, it was observed that the signal intensity characteristics are proportional to the melt pool dimensions and that the signal dynamics characteristics relate to processing conditions known to generate spatter. Hence, even though no correlations between melt pool signal characteristics and content of internal flaws generated systematically were identified, this monitoring system can be employed to detect instabilities that can generate spatters and thereby stochastic flaws elsewhere in the build area (RQ2).

Still in the investigation of detectability of systematic flaws by means of monitoring systems, it was demonstrated that a fully convolutional neural network trained on near-infrared long-exposure images is capable of classifying individual layers of specimens per predominant flaw type in the categories *keyhole porosity*, *lack of fusion*, and *residual porosity* with high accuracy, precision and recall, when considering systematic process parameter-induced flaws. Hence, internal flaws can be detected, categorized and assessed online (RQ1, RQ2).

Upon investigation of detectability of stochastic flaws, it was found that a spatter detector applied on near-infrared long-exposure imaging is capable of identifying regions with high incidence of lack of fusion. Additionally, the spatial distribution of spatter redeposits on the powder bed was elucidated. Differently from systematic flaws, the internal flaws observed in the study of stochastic flaws were not uniformly distributed throughout the material, instead followed a similar pattern as the spatter redeposits detected through the monitoring system. Spherical particles with dendritic structure were observed on specimen cross-sections near lack of fusion. Analysis of the fracture surface revealed particles with size, surface morphology and state of oxidation characteristic of spatter on the adjacencies of lack of fusion. These observations suggest that stochastic lack of fusion can be attributed to spatter redeposited on the build area (RQ3).

CHAPTER 10
FUTURE WORK

Even though it was demonstrated that regions where spatters redeposit are rich in lack of fusion flaws, a one-to-one correspondence between detections and flaws is not yet established. It is still unclear whether all spatter redeposits induce flaws and, if not, which conditions are met when they do. It is also essential to evaluate whether these conditions can be discriminated by analyzing the monitoring system data so that only flaw-generating spatters are flagged in closed-loop control. Furthermore, even if a spatter redeposit at first generates a flaw, it is possible, due to the additive nature of the manufacturing process, to re-process the flaw region and eliminate the flaw. The healing effect can occur unintentionally as a result of the deposition of the subsequent build layers or can be induced by tailoring the melting conditions. These aspects of spatter redeposition will be studied in future work. Furthermore, the evaluation of the effect of internal flaws on the mechanical properties is planned, as well as the effectiveness of different strategies of flaw mitigation, which must be addressed prior to the implementation of closed-loop control. Finally, thus far, only Hastelloy X has been studied. The generalization of the work presented in this thesis to other alloy systems and in detecting other flaws generated in-process is planned.

ACKNOWLEDGEMENTS

I would like to thank my supervisor Professor Lars Nyborg and co-supervisor Professor Eduard Hryha for the opportunity to work on this topic and for all their support. I am especially grateful to Lars for always finding time for me in his busy schedule and for going the extra mile in making this research possible, even though much of the home stretch has taken place during the height of summer. I would also like to thank Professor Antal Boldizar for providing me with insights into how to navigate academia.

I gratefully acknowledge the funding received from Horizon 2020 research and innovation programme through the project MANUELA (Additive Manufacturing using Metal Pilot Line), and from the Centre for Additive Manufacturing (CAM2). Thanks to Electro Optical Systems Finland Oy for providing the feedstock powder utilized in this research.

I would like to acknowledge my colleagues at the Department of Industrial and Materials Science for all their help and for all they taught me in these two years. A special thanks to research engineer Roger Sagdahl for his unfailing and skilled assistance.

A big thanks to my friends and family, close and far away, not the least to Lise-Lott and Hans Ove for all their help in things big and small. I am equally grateful to my fellow Ph.D. students and friends Adriana and Juliano for all the long chats about life as a Ph.D. student and for all their good advice. My sincere thanks to those who have always been there for me: my sister Daniela, Pati, André and Gi, who have all been essential through both ups and downs. Finally, a special thanks to Joel for his immense support, endless patience and for accompanying me on the adventures that provided me with the energy and stamina needed to progress in this research.

REFERENCES

[1] MANUELA - Additive Manufacturing using Metal Pilot Line, (n.d.). https://manuela-project.eu/.

[2] Glossary of Metallurgical and Metalworking Terms, in: Met. Handb. Desk Ed., ASM International, 1998. https://doi.org/10.31399/asm.hb.mhde2.a0005721.

[3] T. DebRoy, H.L. Wei, J.S. Zuback, T. Mukherjee, J.W. Elmer, J.O. Milewski, A.M. Beese, A. Wilson-Heid, A. De, W. Zhang, Additive manufacturing of metallic components – Process, structure and properties, Prog. Mater. Sci. 92 (2018) 112–224. https://doi.org/10.1016/j.pmatsci.2017.10.001.

[4] ASTM F2792 - 12a, Standard Terminology for Additive Manufacturing Technologies, ASTM International, 2012.

[5] W.E. Frazier, Metal additive manufacturing: A review, J. Mater. Eng. Perform. 23 (2014) 1917–1928. https://doi.org/10.1007/s11665-014-0958-z.

[6] I. Gibson, D.W. Rosen, B. Stucker, Additive manufacturing technologies: Rapid prototyping to direct digital manufacturing, Springer US, 2010. https://doi.org/10.1007/978-1-4419-1120-9.

[7] P.G. Klemens, Heat balance and flow conditions for electron beam and laser welding, J. Appl. Phys. 47 (1976) 2165–2174. https://doi.org/10.1063/1.322866.

[8] T. Debroy, S.A. David, Physical processes in fusion welding, Rev. Mod. Phys. 67 (1995). https://doi.org/10.1103/RevModPhys.67.85.

[9] E.A. Metzbower, Keyhole formation, Metall. Trans. B. 24 (1993) 875–880. https://doi.org/10.1007/BF02663148.

[10] R. Rai, J.W. Elmer, T.A. Palmer, T. Debroy, Heat transfer and fluid flow during keyhole mode laser welding of tantalum, Ti-6Al-4V, 304L stainless steel and vanadium, J. Phys. D. Appl. Phys. 40 (2007) 5753–5766. https://doi.org/10.1088/0022-3727/40/18/037.

[11] M. Ma, Z. Wang, M. Gao, X. Zeng, Layer thickness dependence of performance in high-power selective laser melting of 1Cr18Ni9Ti stainless steel, J. Mater. Process. Technol. 215 (2015) 142–150. https://doi.org/10.1016/j.jmatprotec.2014.07.034.

[12] Z. Sun, X. Tan, S.B. Tor, W.Y. Yeong, Selective laser melting of stainless steel 316L with low porosity and high build rates, Mater. Des. (2016). https://doi.org/10.1016/j.matdes.2016.05.035.

[13] C. de Formanoir, U. Paggi, T. Colebrants, L. Thijs, G. Li, K. Vanmeensel, B. Van Hooreweder, Increasing the productivity of laser powder bed fusion: Influence of the hull-bulk strategy on part quality, microstructure and mechanical performance of Ti-6Al-4V, Addit. Manuf. 33 (2020). https://doi.org/10.1016/j.addma.2020.101129.

[14] M. Attaran, The rise of 3-D printing: The advantages of additive manufacturing over traditional manufacturing, Bus. Horiz. 60 (2017) 677–688.

https://doi.org/10.1016/J.BUSHOR.2017.05.011.

[15] A. Leicht, M. Fischer, U. Klement, L. Nyborg, E. Hryha, Increasing the Productivity of Laser Powder Bed Fusion for Stainless Steel 316L through Increased Layer Thickness, J. Mater. Eng. Perform. 30 (2021) 575–584. https://doi.org/10.1007/s11665-020-05334-3.

[16] H. Schleifenbaum, A. Diatlov, C. Hinke, J. Bültmann, H. Voswinckel, Direct photonic production: Towards high speed additive manufacturing of individualized goods, Prod. Eng. 5 (2011) 359–371. https://doi.org/10.1007/s11740-011-0331-0.

[17] D. Buchbinder, H. Schleifenbaum, S. Heidrich, W. Meiners, J. Bültmann, High Power Selective Laser Melting (HP SLM) of Aluminum Parts, Phys. Procedia. 12 (2011) 271–278. https://doi.org/10.1016/j.phpro.2011.03.035.

[18] X. Shi, S. Ma, C. Liu, C. Chen, Q. Wu, X. Chen, J. Lu, Performance of high layer thickness in selective laser melting of Ti6Al4V, Materials (Basel). 9 (2016). https://doi.org/10.3390/ma9120975.

[19] M. Grasso, B.M. Colosimo, Process defects and in situ monitoring methods in metal powder bed fusion: A review, Meas. Sci. Technol. 28 (2017) aa5c4f. https://doi.org/10.1088/1361-6501/aa5c4f.

[20] J.A. Kanko, A.P. Sibley, J.M. Fraser, In situ morphology-based defect detection of selective laser melting through inline coherent imaging, J. Mater. Process. Technol. 231 (2016) 488–500. https://doi.org/10.1016/j.jmatprotec.2015.12.024.

[21] L. Scime, J. Beuth, Using machine learning to identify in-situ melt pool signatures indicative of flaw formation in a laser powder bed fusion additive manufacturing process, Addit. Manuf. 25 (2019) 151–165. https://doi.org/10.1016/j.addma.2018.11.010.

[22] W.E. King, H.D. Barth, V.M. Castillo, G.F. Gallegos, J.W. Gibbs, D.E. Hahn, C. Kamath, A.M. Rubenchik, Observation of keyhole-mode laser melting in laser powder-bed fusion additive manufacturing, J. Mater. Process. Technol. 214 (2014) 2915–2925. https://doi.org/10.1016/j.jmatprotec.2014.06.005.

[23] H. Gong, K. Rafi, H. Gu, T. Starr, B. Stucker, Analysis of defect generation in Ti-6Al-4V parts made using powder bed fusion additive manufacturing processes, Addit. Manuf. 1 (2014) 87–98. https://doi.org/10.1016/j.addma.2014.08.002.

[24] N.T. Aboulkhair, N.M. Everitt, I. Ashcroft, C. Tuck, Reducing porosity in AlSi10Mg parts processed by selective laser melting, Addit. Manuf. 1 (2014) 77–86. https://doi.org/10.1016/j.addma.2014.08.001.

[25] Z. Snow, A.R. Nassar, E.W. Reutzel, Invited Review Article: Review of the formation and impact of flaws in powder bed fusion additive manufacturing, Addit. Manuf. 36 (2020). https://doi.org/10.1016/j.addma.2020.101457.

[26] S. Kou, Welding Metallurgy, 2nd ed., John Wiley & Sons, Inc., 2003.

[27] A. Ladewig, G. Schlick, M. Fisser, V. Schulze, U. Glatzel, Influence of the shielding gas flow on the removal of process by-products in the selective laser melting process, Addit. Manuf. 10 (2016) 1–9. https://doi.org/10.1016/j.addma.2016.01.004.

[28] Y. Liu, Y. Yang, S. Mai, D. Wang, C. Song, Investigation into spatter behavior during

selective laser melting of AISI 316L stainless steel powder, Mater. Des. 87 (2015) 797–806. https://doi.org/10.1016/j.matdes.2015.08.086.

[29] S.A. Khairallah, A.T. Anderson, A. Rubenchik, W.E. King, Laser powder-bed fusion additive manufacturing: Physics of complex melt flow and formation mechanisms of pores, spatter, and denudation zones, Acta Mater. 108 (2016) 36–45. https://doi.org/10.1016/j.actamat.2016.02.014.

[30] S. Ly, A.M. Rubenchik, S.A. Khairallah, G. Guss, M.J. Matthews, Metal vapor micro-jet controls material redistribution in laser powder bed fusion additive manufacturing, Sci. Rep. 7 (2017) 1–12. https://doi.org/10.1038/s41598-017-04237-z.

[31] P. Bidare, I. Bitharas, R.M. Ward, M.M. Attallah, A.J. Moore, Fluid and particle dynamics in laser powder bed fusion, Acta Mater. 142 (2018) 107–120. https://doi.org/10.1016/j.actamat.2017.09.051.

[32] Z.A. Young, Q. Guo, N.D. Parab, C. Zhao, M. Qu, L.I. Escano, K. Fezzaa, W. Everhart, T. Sun, L. Chen, Types of spatter and their features and formation mechanisms in laser powder bed fusion additive manufacturing process, Addit. Manuf. 36 (2020) 101438. https://doi.org/10.1016/j.addma.2020.101438.

[33] D. Wang, S. Wu, F. Fu, S. Mai, Y. Yang, Y. Liu, C. Song, Mechanisms and characteristics of spatter generation in SLM processing and its effect on the properties, Mater. Des. 117 (2017) 121–130. https://doi.org/10.1016/j.matdes.2016.12.060.

[34] M. Simonelli, C. Tuck, N.T. Aboulkhair, I. Maskery, I. Ashcroft, R.D. Wildman, R. Hague, A Study on the Laser Spatter and the Oxidation Reactions During Selective Laser Melting of 316L Stainless Steel, Al-Si10-Mg, and Ti-6Al-4V, Metall. Mater. Trans. A Phys. Metall. Mater. Sci. 46 (2015) 3842–3851. https://doi.org/10.1007/s11661-015-2882-8.

[35] R. Esmaeilizadeh, U. Ali, A. Keshavarzkermani, Y. Mahmoodkhani, E. Marzbanrad, E. Toyserkani, On the effect of spatter particles distribution on the quality of Hastelloy X parts made by laser powder-bed fusion additive manufacturing, J. Manuf. Process. 37 (2019) 11–20. https://doi.org/10.1016/j.jmapro.2018.11.012.

[36] M. Tang, P.C. Pistorius, Oxides, porosity and fatigue performance of AlSi10Mg parts produced by selective laser melting, Int. J. Fatigue. 94 (2017) 192–201. https://doi.org/10.1016/j.ijfatigue.2016.06.002.

[37] S. Beretta, S. Romano, A comparison of fatigue strength sensitivity to defects for materials manufactured by AM or traditional processes, Int. J. Fatigue. 94 (2017) 178–191. https://doi.org/10.1016/j.ijfatigue.2016.06.020.

[38] ASM Handbook, Volume 11, Failure Analysis and Prevention, 2002. http://books.google.com.hk/books?id=eC-Zt1J4oCgC.

[39] L. Scime, J. Beuth, Anomaly detection and classification in a laser powder bed additive manufacturing process using a trained computer vision algorithm, Addit. Manuf. 19 (2018) 114–126. https://doi.org/10.1016/j.addma.2017.11.009.

[40] J.L. Bartlett, A. Jarama, J. Jones, X. Li, Prediction of microstructural defects in additive manufacturing from powder bed quality using digital image correlation, Mater. Sci. Eng. A. 794 (2020). https://doi.org/10.1016/j.msea.2020.140002.

[41] Q.Y. Lu, N.V. Nguyen, A.J.W. Hum, T. Tran, C.H. Wong, Identification and

evaluation defects in selective laser melted 316 L stainless steel parts via in-situ monitoring and micro computed tomography, Addit. Manuf. 35 (2020) 101287. https://doi.org/10.1016/j.addma.2020.101287.

[42] C. Gobert, E.W. Reutzel, J. Petrich, A.R. Nassar, S. Phoha, Application of supervised machine learning for defect detection during metallic powder bed fusion additive manufacturing using high resolution imaging., Addit. Manuf. 21 (2018) 517–528. https://doi.org/10.1016/j.addma.2018.04.005.

[43] F. Imani, A. Gaikwad, M. Montazeri, P. Rao, H. Yang, E. Reutzel, Process mapping and in-process monitoring of porosity in laser powder bed fusion using layerwise optical imaging, J. Manuf. Sci. Eng. Trans. ASME. 140 (2018). https://doi.org/10.1115/1.4040615.

[44] A. Caggiano, J. Zhang, V. Alfieri, F. Caiazzo, R. Gao, R. Teti, Machine learning-based image processing for on-line defect recognition in additive manufacturing, CIRP Ann. 68 (2019) 451–454. https://doi.org/10.1016/j.cirp.2019.03.021.

[45] C.K. Chua, C.H. Wong, W.Y. Yeong, Process Control and Modeling, in: Stand. Qual. Control. Meas. Sci. 3D Print. Addit. Manuf., Elsevier, 2017: pp. 159–179. https://doi.org/10.1016/b978-0-12-813489-4.00007-6.

[46] S. Clijsters, T. Craeghs, S. Buls, K. Kempen, J.P. Kruth, In situ quality control of the selective laser melting process using a high-speed, real-time melt pool monitoring system, Int. J. Adv. Manuf. Technol. 75 (2014) 1089–1101. https://doi.org/10.1007/s00170-014-6214-8.

[47] T. Craeghs, S. Clijsters, J.P. Kruth, F. Bechmann, M.C. Ebert, Detection of Process Failures in Layerwise Laser Melting with Optical Process Monitoring, in: Phys. Procedia, Elsevier B.V., 2012: pp. 753–759. https://doi.org/10.1016/j.phpro.2012.10.097.

[48] M. Bisht, N. Ray, F. Verbist, S. Coeck, Correlation of selective laser melting-melt pool events with the tensile properties of Ti-6Al-4V ELI processed by laser powder bed fusion, Addit. Manuf. 22 (2018) 302–306. https://doi.org/10.1016/j.addma.2018.05.004.

[49] S. Coeck, M. Bisht, J. Plas, F. Verbist, Prediction of lack of fusion porosity in selective laser melting based on melt pool monitoring data, Addit. Manuf. 25 (2019) 347–356. https://doi.org/10.1016/j.addma.2018.11.015.

[50] J.B. Forien, N.P. Calta, P.J. DePond, G.M. Guss, T.T. Roehling, M.J. Matthews, Detecting keyhole pore defects and monitoring process signatures during laser powder bed fusion: A correlation between in situ pyrometry and ex situ X-ray radiography, Addit. Manuf. 35 (2020). https://doi.org/10.1016/j.addma.2020.101336.

[51] Y. Zhang, G.S. Hong, D. Ye, K. Zhu, J.Y.H. Fuh, Extraction and evaluation of melt pool, plume and spatter information for powder-bed fusion AM process monitoring, Mater. Des. 156 (2018) 458–469. https://doi.org/10.1016/j.matdes.2018.07.002.

[52] D. Ye, G.S. Hong, Y. Zhang, K. Zhu, J.Y.H. Fuh, Defect detection in selective laser melting technology by acoustic signals with deep belief networks, Int. J. Adv. Manuf. Technol. 96 (2018) 2791–2801. https://doi.org/10.1007/s00170-018-1728-0.

[53] S.A. Shevchik, C. Kenel, C. Leinenbach, K. Wasmer, Acoustic emission for in situ

quality monitoring in additive manufacturing using spectral convolutional neural networks, Addit. Manuf. 21 (2018) 598–604. https://doi.org/10.1016/j.addma.2017.11.012.

[54] I. Yadroitsev, P. Krakhmalev, I. Yadroitsava, Selective laser melting of Ti6Al4V alloy for biomedical applications: Temperature monitoring and microstructural evolution, J. Alloys Compd. 583 (2014) 404–409. https://doi.org/10.1016/j.jallcom.2013.08.183.

[55] H. Baumgartl, J. Tomas, R. Buettner, M. Merkel, A deep learning-based model for defect detection in laser-powder bed fusion using in-situ thermographic monitoring, Prog. Addit. Manuf. 5 (2020) 277–285. https://doi.org/10.1007/s40964-019-00108-3.

[56] M. Khanzadeh, S. Chowdhury, M.A. Tschopp, H.R. Doude, M. Marufuzzaman, L. Bian, In-situ monitoring of melt pool images for porosity prediction in directed energy deposition processes, IISE Trans. 51 (2019) 437–455. https://doi.org/10.1080/24725854.2017.1417656.

[57] B.E. Adams, C.W. Schietinger, K.G. Kreider, Radiation Thermometry in the Semiconductor Industry, Exp. Methods Phys. Sci. 43 (2010) 137–216. https://doi.org/10.1016/S1079-4042(09)04303-3.

[58] J.A. Mitchell, T.A. Ivanoff, D. Dagel, J.D. Madison, B. Jared, Linking pyrometry to porosity in additively manufactured metals, Addit. Manuf. 31 (2020). https://doi.org/10.1016/j.addma.2019.100946.

[59] G. Mohr, S.J. Altenburg, A. Ulbricht, P. Heinrich, D. Baum, C. Maierhofer, K. Hilgenberg, In-situ defect detection in laser powder bed fusion by using thermography and optical tomography—comparison to computed tomography, Metals (Basel). 10 (2020). https://doi.org/10.3390/met10010103.

[60] M. Abdelrahman, E.W. Reutzel, A.R. Nassar, T.L. Starr, Flaw detection in powder bed fusion using optical imaging, Addit. Manuf. 15 (2017) 1–11. https://doi.org/10.1016/j.addma.2017.02.001.

[61] H. Kong, H.C. Akakin, S.E. Sarma, A generalized laplacian of gaussian filter for blob detection and its applications, IEEE Trans. Cybern. 43 (2013) 1719–1733. https://doi.org/10.1109/TSMCB.2012.2228639.

[62] Y. LeCun, L. Bottou, Y. Bengio, P. Haffner, Gradient-based learning applied to document recognition, Proc. IEEE. 86 (1998) 2278–2323. https://doi.org/10.1109/5.726791.

[63] M.D. Zeiler, R. Fergus, LNCS 8689 - Visualizing and Understanding Convolutional Networks, 2014.

[64] R.C. Reed, The Superalloys Fundamentals and Applications, Cambridge University Press, 2006. www.cambridge.org /9780521859042.

[65] ASM Metals Handbook, Volume 2, Properties and Selection: Nonferrous Alloys and Special-Purpose Materials, ASM International, 1990. https://doi.org/10.31399/asm.hb.v02.9781627081627.

[66] ASM Metals Handbook, Volume 9, Metallography and Microstructures, ASM International, 2004. https://doi.org/10.31399/asm.hb.v09.9781627081771.

[67] Haynes International, (n.d.). https://www.haynesintl.com/alloys/alloy-portfolio_/High-

temperature-Alloys/HASTELLOY-X-alloy.

[68] Y.M. Wang, T. Voisin, J.T. McKeown, J. Ye, N.P. Calta, Z. Li, Z. Zeng, Y. Zhang, W. Chen, T.T. Roehling, R.T. Ott, M.K. Santala, P.J. Depond, M.J. Matthews, A. V. Hamza, T. Zhu, Additively manufactured hierarchical stainless steels with high strength and ductility, Nat. Mater. 2017 171. 17 (2017) 63–71. https://doi.org/10.1038/nmat5021.

[69] M.L. Montero-Sistiaga, Z. Liu, L. Bautmans, S. Nardone, G. Ji, J.P. Kruth, J. Van Humbeeck, K. Vanmeensel, Effect of temperature on the microstructure and tensile properties of micro-crack free hastelloy X produced by selective laser melting, Addit. Manuf. 31 (2020) 100995. https://doi.org/10.1016/J.ADDMA.2019.100995.

[70] Q. Han, R. Mertens, M.L. Montero-Sistiaga, S. Yang, R. Setchi, K. Vanmeensel, B. Van Hooreweder, S.L. Evans, H. Fan, Laser powder bed fusion of Hastelloy X: Effects of hot isostatic pressing and the hot cracking mechanism, Mater. Sci. Eng. A. 732 (2018) 228–239. https://doi.org/10.1016/j.msea.2018.07.008.

[71] D. Tomus, P.A. Rometsch, M. Heilmaier, X. Wu, Effect of minor alloying elements on crack-formation characteristics of Hastelloy-X manufactured by selective laser melting, Addit. Manuf. 16 (2017) 65–72. https://doi.org/10.1016/j.addma.2017.05.006.

[72] N.J. Harrison, I. Todd, K. Mumtaz, Reduction of micro-cracking in nickel superalloys processed by Selective Laser Melting: A fundamental alloy design approach, Acta Mater. 94 (2015) 59–68. https://doi.org/10.1016/j.actamat.2015.04.035.

[73] G. Marchese, G. Basile, E. Bassini, A. Aversa, M. Lombardi, D. Ugues, P. Fino, S. Biamino, Study of the microstructure and cracking mechanisms of hastelloy X produced by laser powder bed fusion, Materials (Basel). 11 (2018). https://doi.org/10.3390/ma11010106.

[74] O. Sanchez-Mata, X. Wang, J.A. Muñiz-Lerma, M.A. Shandiz, R. Gauvin, M. Brochu, Fabrication of crack-free nickel-based superalloy considered non-weldable during laser powder bed fusion, Materials (Basel). 11 (2018) 1–9. https://doi.org/10.3390/ma11081288.

[75] O. Sanchez-Mata, J.A. Muñiz-Lerma, X. Wang, S.E. Atabay, M. Attarian Shandiz, M. Brochu, Microstructure and mechanical properties at room and elevated temperature of crack-free Hastelloy X fabricated by laser powder bed fusion, Mater. Sci. Eng. A. 780 (2020). https://doi.org/10.1016/j.msea.2020.139177.

[76] X. Ni, D. Kong, L. Zhang, C. Dong, J. Song, W. Wu, Effect of Process Parameters on the Mechanical Properties of Hastelloy X Alloy Fabricated by Selective Laser Melting, J. Mater. Eng. Perform. 28 (2019) 5533–5540. https://doi.org/10.1007/s11665-019-04275-w.

[77] T.H.C. Childs, C. Hauser, M. Badrossamay, Selective laser sintering (melting) of stainless and tool steel powders: Experiments and modelling, Proc. Inst. Mech. Eng. Part B J. Eng. Manuf. 219 (2005) 339–357. https://doi.org/10.1243/095440505X8109.

[78] 3D Printing Software EOSTATE - EOS Monitoring & Quality Assurance for Production with Additive Manufacturing, (n.d.). https://www.eos.info/en/additive-manufacturing/software-3d-printing/monitoring-software#meltpool.

[79] Y. Yamashita, T. Murakami, R. Mihara, M. Okada, Y. Murakami, Defect Analysis and

Fatigue Design Basis for Ni-based Superalloy 718 manufactured by Additive Manufacturing, Procedia Struct. Integr. 7 (2017) 11–18. https://doi.org/10.1016/j.prostr.2017.11.054.

[80] L. Nyborg, A. Nylund, I. Olefjord, Thickness determination of oxide layers on spherically-shaped metal powders by ESCA, Surf. Interface Anal. 12 (1988) 110–114. https://doi.org/10.1002/sia.740120209.

[81] R. Kelly, N.Q. Lam, Sputtering of oxides. I. A Survey of the experimental results, (1973). http://inis.iaea.org/Search/search.aspx?orig_q=RN:6193004 (accessed July 22, 2021).